ACS Catalysis

Research Article

Cite This: ACS Catal. 2018, 8, 7051−7067

pubs.acs.org/acscatalysis

Influence of Tight Confinement on Selective Oxidative Dehydrogenation of Ethane on MoVTeNb Mixed Oxides

Leelavathi Annamalai,[†,∥] Yilang Liu,[†,∥] Sopuruchukwu Ezenwa,[†] Yanliu Dang,[§] Steven L Suib,[‡,§] and Prashant Deshlahra*[,†]

[†]Department of Chemical and Biological Engineering, Tufts University, Medford, Massachusetts 02155, United States

[§]Institute of Materials Science, University of Connecticut, Storrs, Connecticut 06269, United States

[‡]Department of Chemistry, University of Connecticut, Storrs, Connecticut 06269, United States

Supporting Information

ABSTRACT: M1 phase MoVTeNb mixed oxides exhibit unique catalytic properties that lead to high C_2H_4 yields in oxidative conversion of C_2H_6 at moderate temperatures. The role of the heptagonal channel micropores of the M1 phase in regulating reactivity and selectivity is assessed here using reactant size-dependent kinetic probes and density functional theory (DFT) treatments for C_2H_6 and cyclohexane (C_6H_{12}) activations inside and outside the micropores. The sizes of C_2H_6 and the micropores suggest a tight guest−host fit, but C_6H_{12} cannot access intrapore sites. Measured C_2H_6 to C_6H_{12} activation rate ratios on MoVTeNbO are much higher than those measured on nonmicroporous vanadium oxides (VO_x/SiO_2) and estimated by DFT on external surfaces, suggesting that most C_2H_6 activations on MoVTeNbO occur inside the micropores under typical conditions. C_2H_6 exhibits higher activation energy than C_6H_{12} on VO_x/SiO_2, consistent with the corresponding C−H bond strengths; the activation energy difference between C_2H_6 and C_6H_{12} is lower on MoVTeNbO because micropores stabilize C−H activation transition states through van der Waals interactions. Product selectivities for C_2H_6 and C_6H_{12} suggest that the ability of VO_x/SiO_2 to activate C−H bonds and resist O-insertion in products is similar to the external surfaces of MoVTeNbO, but the micropores in the latter oxides are more selective for C−H activation. DFT calculations show that the tight confinement in micropores hinders the C−O contact necessary for O-insertion. These insights provide guidance for utilizing shapes and sizes of confining voids to mitigate selectivity limitations dictated by thermodynamics of sequential oxidation reactions and electronic properties of redox catalysts.

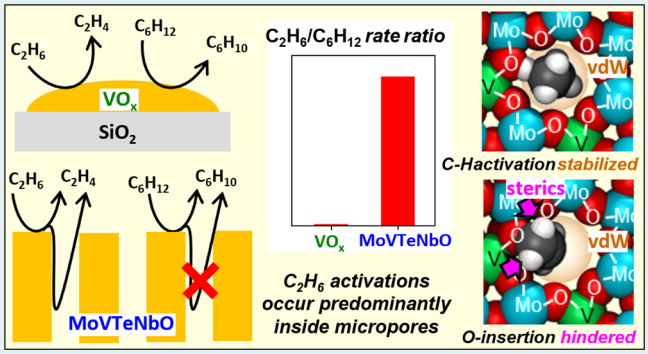

KEYWORDS: *C−H activation, O-insertion, M1 phase, selective oxidation, van der Waals interactions, steric hindrance*

1. INTRODUCTION

Oxidative dehydrogenation (ODH) of small alkanes provides an important energy-efficient route to the production of alkenes that constitute essential building blocks of the chemical industry.[1,2] Mixed bulk oxides of Mo, V, Nb, Te, and other elements (Sb, Ta, and W),[3] arranged in an orthorhombic crystalline form, known as the M1 phase, catalyze ethane ODH with exceptionally high selectivity to ethylene at moderate reaction temperatures.[4−9] These oxides also play an important role in selective formation of acrolein, acrylic acid, or acrylonitrile directly from a propane feed, instead of the more conventional propene-based processes.[10−14] Relations among synthesis methods, structures, and catalytic functions of these solids are being probed extensively.[15−24]

The M1 phase oxides consist of layers of interconnected octahedral Mo and V oxo groups stacked along the [001] direction. The arrangements of octahedra in (001) planes form pentagonal, hexagonal, and heptagonal rings (Scheme 1),[17,25] which lead to one-dimensional pores in the stacked solids. The pentagonal and hexagonal pores are typically occupied by cations, and their sizes are smaller than the smallest organic molecules. In contrast, the heptagonal pores remain at least partially open and potentially accessible to small reactants.[19,26] The numbers and valences of metal cations and oxoanions and crystallographic analysis of distortions of oxo octahedra via bond valence sum calculations suggest that the framework contains a combination of fully oxidized (V^{5+} and Mo^{6+}) and partially reduced (V^{4+} and Mo^{5+}) cations.[27]

The reactivity of MoVTeNb oxides for ethane ODH has been attributed to (001) M1 planes[28−33] or a combination of different exposed facets of crystallites.[20] Within the (001) planes, the oxo species connected to V cations were

Received: April 23, 2018
Revised: June 15, 2018
Published: July 5, 2018

DOI: 10.1021/acscatal.8b01586
ACS Catal. 2018, 8, 7051−7067

Scheme 1. Two Dimensional Polyhedral Representation of the M1 Phase of MoVTeNbO[a]

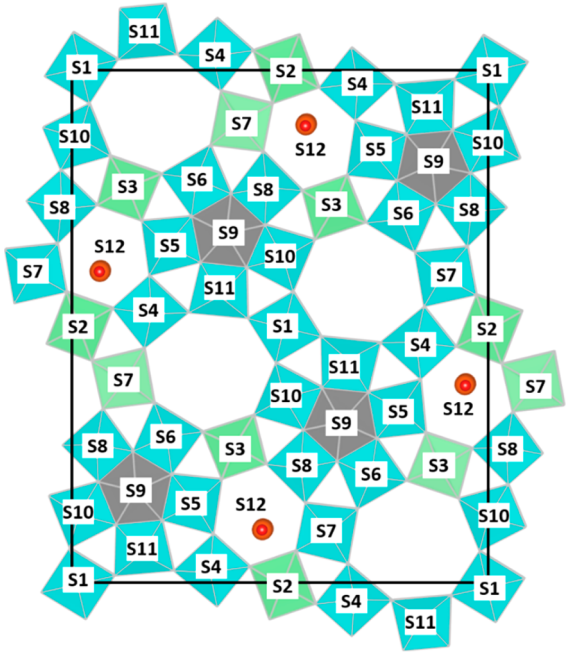

[a]Mo sites and V sites are shown as blue and green octahedra, respectively (S1−S8, S10, and S11). Nb sites are shown as gray pentagonal bipyramids (S9). Te sites are shown as orange spheres (S12).

determined to be the active sites.[31−33] Other more reactive sites at oxo species connected to Te and surface O-radicals generated via dynamic reduction and removal of Te atoms from the lattice have also been proposed.[15,21] Differences between surface and bulk compositions and their influence on oxygenate selectivity in oxidative conversion of propane have been reported and attributed to distinct roles of surface monolayers and underlying bulk structure.[34−36] The selective nature of these oxides toward specific oxidation products has been attributed to a "site isolation principle," which proposes that reactive V^{5+} cations isolated within a matrix of less reactive centers prevent overoxidation of products generated at an isolated site.[27,37] Details of how the identified catalytic sites selectively activate C−H bonds in alkanes and why the alkene products originated from one isolated site do not undergo secondary reactions on other isolated sites in the system remain speculative.

In contrast to the external reactive sites identified for MoVTeNb oxides, ethane activations on M1 phase MoV oxides are proposed to occur inside the heptagonal pores.[38] These pores are of the same size as the kinetic diameter of ethane (0.4 nm)[38,39] and are accessible to ethane, as determined from atom-resolved microscopy and adsorption isotherms, respectively.[19,40,41] Ethane ODH rates on MoV samples of different crystallite sizes were proportional to the micropore volume and independent of the external area.[38] In spite of identical heptagonal pores in MoV and MoVTeNb oxides, few studies focused on the catalytic relevance of pores in the latter material. Moreover, the origin of the selective nature of ODH reactions within the pores for both types of oxides has remained unaddressed.

Pores of molecular dimensions in aluminosilicates and other zeotype materials control reactivity and selectivity via dispersion forces and steric restrictions that vary with shapes and sizes of reactants and transition states.[42,43] Analogous size selectivity effects have been achieved via deposition of molecular-scale sieving patterns of inert overlayers on nonporous reactive oxides.[44] The catalytic effects of the pores of bulk transition metal oxide crystals and their physical origins and mechanistic connections to selective hydrocarbon activation catalysis have not been identified.

Here, we demonstrate the importance of heptagonal micropores of MoVTeNb oxide in selective C−H activation using measured rates and density functional theory (DFT) derived energetics for oxidative conversions of ethane (C_2H_6) and cyclohexane (C_6H_{12}). The size of C_6H_{12} restricts its reactions to external surfaces of oxides, but C_2H_6 molecules react predominantly within the heptagonal pores, as indicated by C_2H_6/C_6H_{12} activation rate ratios that are more than 2 orders of magnitude larger than the ratios on nonmicroporous silica supported vanadium oxide. C−H activation energies, selectivity to alkenes, and computed energies and structures of relevant surface species suggest that micropores tightly confine C_2H_6 molecules and stabilize C−H activation transition states via van der Waals interactions but destabilize undesired O-insertions due to steric hindrance to proximate C−O contact in concave pore walls.

2. METHODS

2.1. Synthesis of Bulk MoVTeNb Oxides and Supported Vanadium Oxides. All metal precursors were purchased from Sigma-Aldrich and used without further purification. The MoVTeNb oxides (MoVTeNbO) were prepared using hydrothermal methods. Ammonium molybdate tetrahydrate (9.72 g, 81−83% MoO_3 basis) was dissolved in deionized water (75 cm^3) at ambient conditions. Vanadyl sulfate (2.31 g, 97%), telluric acid (2.15 g, 99%), and ammonium niobate oxalate hydrate (1.99 g, 99.99%) were added to this solution under continuous stirring, leading to a dark violet solution with a typical reported composition of 1:0.25:0.17:0.12 Mo:V:Te:Nb atomic ratios.[5] After continuous stirring for 0.5 h, this solution was transferred to a 100 cm^3 Teflon vessel, which was sealed in a stainless steel autoclave and treated at 448 K for 48 h in a preheated muffle furnace. The solid products were washed with deionized water and dried overnight in an oven maintained at 373 K. The dried solids were treated in flowing He (50 cm^3 min^{-1} 99.999%, Airgas) in a tube furnace ramped to 873 at 0.083 K s^{-1} and held for 2 h. Another procedure involving slightly different precursor composition and hydrothermal treatment at 403 K for 96 h was used for comparison,[45] as described in Section S2.

Vanadium oxide dispersed on SiO_2 (VO_x/SiO_2) was prepared using wet impregnation. Oxalic acid (2.94 g; Sigma-Aldrich, ≥99%) was dissolved in deionized water (196 cm^3) at ambient temperature and ammonium metavanadate (1.96 g; 99%) was added under continuous stirring to obtain a solution with 1:1.5:100 oxalic acid:V:H_2O molar ratios. SiO_2 powder (2.5 g; Sigma-Aldrich (Davisil grade 633, ≥99%, 480 m^2 g^{-1}) was added to the solution, and the resulting mixture was stirred at 373 K for 0.5 h to form a slurry that was dried overnight at 373 K in an oven and treated in flowing air (50 cm^3 min^{-1}) in a tube furnace ramped to 873 at 0.083 K s^{-1} and held for 6 h.

2.2. Catalyst Characterization. Powder X-ray diffraction (XRD) measurements were performed in a Rigaku SmartLab diffractometer using monochromatic Cu Kα radiation (1.542 Å

DOI: 10.1021/acscatal.8b01586
ACS Catal. 2018, 8, 7051−7067

wavelength) and scans of 0.05° step sizes. The morphology of MoVTeNb oxides was inspected using a Zeiss Ultra 55, field emission scanning electron microscope (SEM) operated at 5 kV acceleration with secondary electron detection. A JEOL T20 transmission electron microscope (TEM) operating at 200 kV was used to obtain bright field micrographs and high-resolution TEM images of samples deposited on carbon coated 200 mesh copper grids using ethanol suspensions. N_2 adsorption isotherms were measured at 77 K using a Quantachrome Autosorb iQ2 analyzer after pretreating the samples in flowing He at 573 K for 3 h. The adsorption data were used to estimate micropore volumes and determine external surface areas of crystallites using Brunauer−Emmett−Teller (BET) analysis. The elemental compositions of the catalysts were determined using an inductively coupled plasma atomic emission spectrometer (ICP-AES, Leeman laboratories PS-1000). Samples were ground using mortar and pestle prior to XRD, microscopy, and gas absorption measurements.

2.3. Rate and Selectivity Measurements. The catalysts, as prepared or after mixing with diluent SiO_2, were pressed, crushed, and sieved to retain 106−180 μm aggregates that were placed as vertical fixed beds in a U-tube quartz reactor and heated using a resistive furnace (National Element). Temperatures were measured using a K-type thermocouple (Omega) placed within a dimple at the reactor wall and set using an electronic temperature controller (Watlow, EZ-ZONE). Mass flow controllers (Porter 601 CV Series II) were used to supply gaseous reactants and He. C_6H_{12} (99.9%, Sigma-Aldrich) was evaporated into O_2/He streams using a liquid syringe pump (Cole Parmer, Model 100). Samples (0.07−0.8 g) were heated to reaction temperatures at 0.25 K s^{-1} in flowing He prior to the introduction of reactant mixtures containing C_2H_6 (99.9%, Airgas; 1−8 kPa) or C_6H_{12} (99.9%, Sigma-Aldrich; 1−8 kPa), O_2 (99.999%, Airgas; 1−15 kPa), and He (99.999%, Airgas). All the transfer lines were kept above 363 K to avoid condensation of reactants and products.

An online gas chromatograph (GC, Agilent 7890B) was used to inject reactor effluents into a carboxen-1000 packed column (10′, 1/8" tube, 60/80 mesh) to separate CO, CO_2, O_2, and HCHO for measurement using a thermal conductivity detector, and simultaneously into an HP-PLOT Q (30 mm × 0.32 mm × 20.00 μm capillary) or an HP-1 ms column (30 mm × 0.32 mm × 1.00 μm capillary) to separate C_2H_6 or C_6H_{12}, respectively, and their other oxidation products, for measurement using a flame ionization detector. C_2H_4, CH_3CHO, CO, and CO_2 were the only products detected for C_2H_6 ODH. Cyclohexene (C_6H_{10}), adipic acid ($C_6H_{10}O_4$), cyclohexanone ($C_6H_{10}O$), cyclohexenol ($C_6H_{10}O$), benzene (C_6H_6), CO, and CO_2 were detected for C_6H_{12} ODH. The GC response factors of all detected species were determined via injections at ranges of concentrations relevant to measured conversions. Carbon balances in all reactions were above 97% in all measurements. Blank reactors at highest temperature and conditions representative of kinetic measurements gave negligible conversions for C_2H_6 (<0.01%, 733 K, 3 kPa C_2H_6, 3 kPa O_2 30 cm^3 min^{-1}) and C_6H_{12} (<0.1%, 648 K, 3 kPa C_2H_6, 3 kPa O_2 30 cm^3 min^{-1}). ODH rates on VO_x/SiO_2 decreased continuously with time on stream possibly due to agglomeration of VO_x domains (7% and 20% decrease for C_2H_6 at 648 K and C_6H_{12} at 603 K, respectively, during the initial 1 h; Figure S2a). In contrast, rates on MoVTeNbO samples exhibited an initial increase for C_2H_6, as previously reported,[41,46] and decrease for C_6H_{12} but were more stable than VO_x/SiO_2 at longer times. The kinetic effects of reactant concentrations on rates were determined by measuring conversions at a reference condition at regular intervals (3 kPa C_2H_6 or C_6H_{12}, 3 kPa O_2, 30 cm^3 min^{-1}) to estimate changes in numbers of active sites that were used to normalize rates at other conditions at intermediate times.

2.4. Computational Methods and Models. Periodic density functional theory (DFT) calculations were performed within the Vienna ab initio Simulation Package (VASP)[47−49] using vdW-DF2[50,51] and PBE[52] exchange correlation functionals, plane-wave basis set expansions to 400 eV cutoff energies, and the projector augmented wave (PAW) method[53] to account for electron−core interactions. Spin-polarized electronic structures were converged self-consistently to energy differences less than 1×10^{-5} eV between successive iterative steps. Gaussian smearing was imposed for electron distributions near the Fermi level (width 0.02 eV), and energies were extrapolated to zero smearing. The DFT+U corrections frequently employed for materials with large band-gaps, which may consistently shift reduction energies without affecting relevant relative values, were not used because significant d-electron densities in MoVTeNbO lead to continuous transition from filled to empty bands without apparent gaps (density of states shown in Figure S3).[54]

Scheme 1 shows crystallographically unique metal sites (S1−S12) contained in a unit cell of the M1 phase;[14] previous computational screening studies concluded that V occupation site preference in the network of Mo sites follows the order S2 > S3 > S7 > S4 ≈ S1.[18] Periodic supercells with a single oxide layer and vacuum separation between (001) planes and with two continuous layers were used to represent the external surface and the bulk of the M1 phase, respectively (Figure 1).

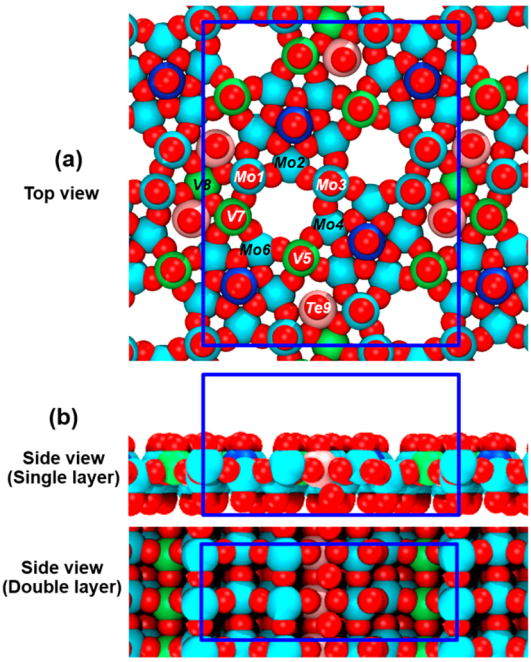

Figure 1. (a) Top and (b) side views of optimized MoVTeNbO structural model with single layer ($Mo_{28}V_8Te_4Nb_4O_{116}$) representing the exposed external surfaces and double layer ($Mo_{56}V_{16}Te_8Nb_8O_{232}$) representing the bulk M1 phase. Blue rectangles represent periodic supercell boundaries. V-atoms occupy S2, S3 and half of S7 sites shown in Scheme 1.

DOI: 10.1021/acscatal.8b01586
ACS Catal. 2018, 8, 7051−7067

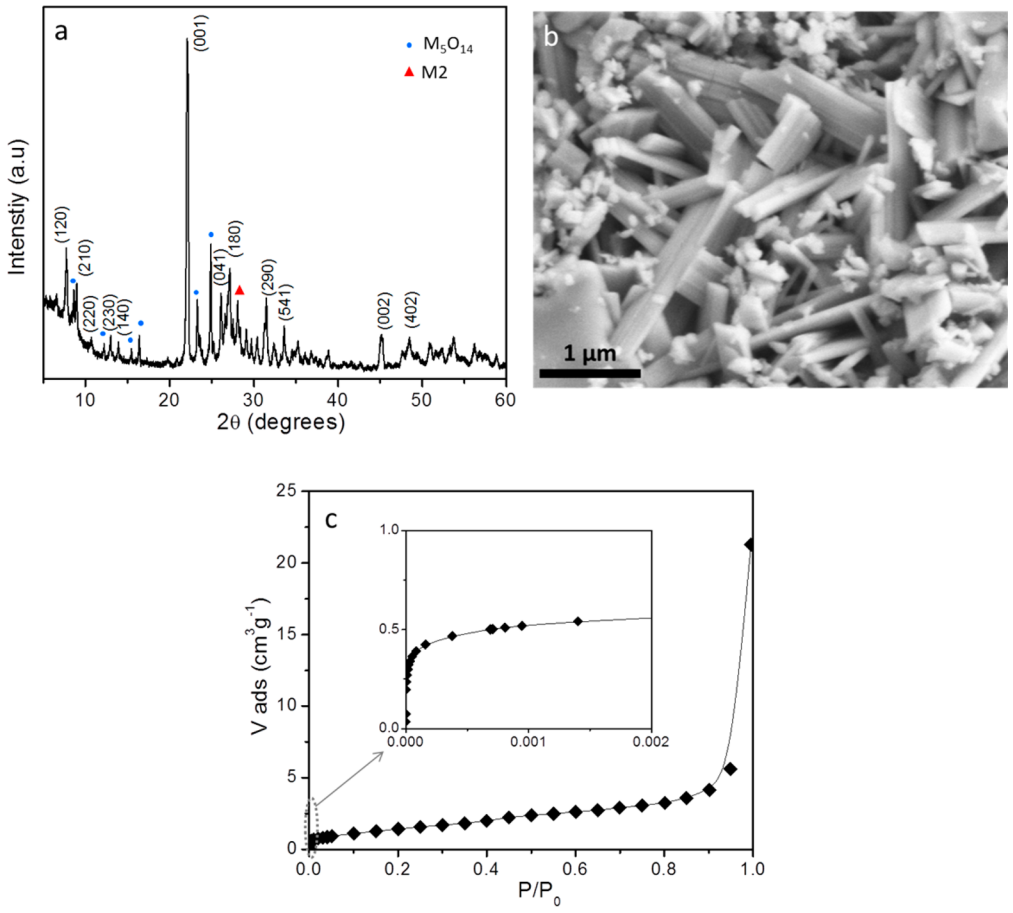

Figure 2. (a) XRD pattern, (b) SEM image, and (c) N_2 adsorption isotherm at 77 K for MoVTeNbO samples. Unlabeled peaks in (a) correspond to positions for multiple Miller indices in the M1 phase. Inset in (c) shows micropore filling at low P/P_0 values (0−0.002).

The single-layer model contains 28 Mo, 8 V, 4 Te, 4 Nb, and 116 O-atoms, leading to V:Mo ratios (0.29) near values measured in catalyst samples (0.27) with complete S2 and S3 and 50% S7 site occupation by V; the double-layer model contained identical atom positions in each layer. The respective supercell dimensions were 21.37 × 26.94 × 12.00 Å and 21.37 × 26.94 × 8.12 Å and the first Brillouin zone was sampled using 1 × 1 × 1 and 1 × 1 × 2 Monkhorst−Pack[55] *k*-point meshes (Figure 1). Structures of transition states were determined using nudged elastic band (NEB) calculations[56] followed by dimer calculations.[57] All structures were optimized until forces on atoms were less than 0.05 eV.

Vibrational frequencies were calculated via diagonalization of Hessians generated from two-sided finite differences of energy gradients obtained by perturbing atoms by 0.01 Å in Cartesian directions. Enthalpies, entropies, and Gibbs free energies were determined from ideal gas statistical mechanics formalisms (details in Section S14).[58] Low frequency vibrational modes (<100 cm^{-1}) of weakly bound molecules, which lead to significant inaccuracies in their contribution to thermodynamic partition functions, were excluded. They were replaced by a fraction (0.7) of gas-phase translational and rotational contributions of these molecules because experiments suggest that weak adsorbates retain nearly 70% of their gas phase entropy on oxides.[59]

3. RESULTS AND DISCUSSION

3.1. Composition and Structure of MoVTeNbO and VO_x/SiO_2. The bulk composition of MoVTeNbO determined from ICP-AES measurements corresponds to a $Mo_1V_{0.27}Te_{0.02}Nb_{0.09}$ stoichiometry with significantly lower Te content than the precursor solution ($Mo_1V_{0.25}Te_{0.17}Nb_{0.12}$), which is consistent with previously reported Te loss during thermal treatments under some synthesis conditions.[60,46] The VO_x/SiO_2 samples contain 41% wt. V_2O_5, based on measured V concentrations, which corresponds to theoretical surface densities of 9.6 V/nm^2 on SiO_2 (480 m^2 g^{-1}). These high V loadings, however, typically exhibit pore blocking, leading to lower dispersions than theoretical values.[61]

The XRD pattern of MoVTeNbO shows the most intense peak at a 2θ value of 22.1° (Figure 2a), which corresponds to the distance between (001) planes in the M1 phase (0.4 nm). Other prominent peaks labeled by their Miller indices are consistent with the orthorhombic M1 phase (ICSD 55097),[62] but minor peaks corresponding to a hexagonal M2 phase (ICSD 55098)[62] and a tetragonal M_5O_{14} phase were also detected (Figure 2a).[63] Thus, the synthesized solids contain the M1 phase together with minority impurity phases and any undetected minor amorphous impurities. The size of micropores in these impurity phases are much smaller than the heptagonal pores of the M1 phase and are inaccessible to ethane molecules, as shown by their atomic arrangements depicted in Figure S4. Amorphous impurities also cannot contain ordered micropores that are selectively accessible to

DOI: 10.1021/acscatal.8b01586
ACS Catal. 2018, 8, 7051−7067

Scheme 2. (a) Kinetic Diameters of Reactants,[38,70] and Accessibility of Surface Catalytic Sites to Reactants on (b) VO_x/SiO_2 and (c) MoVTeNbO

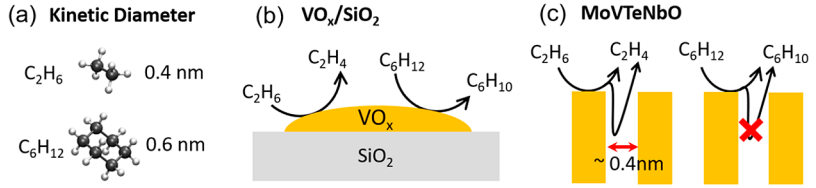

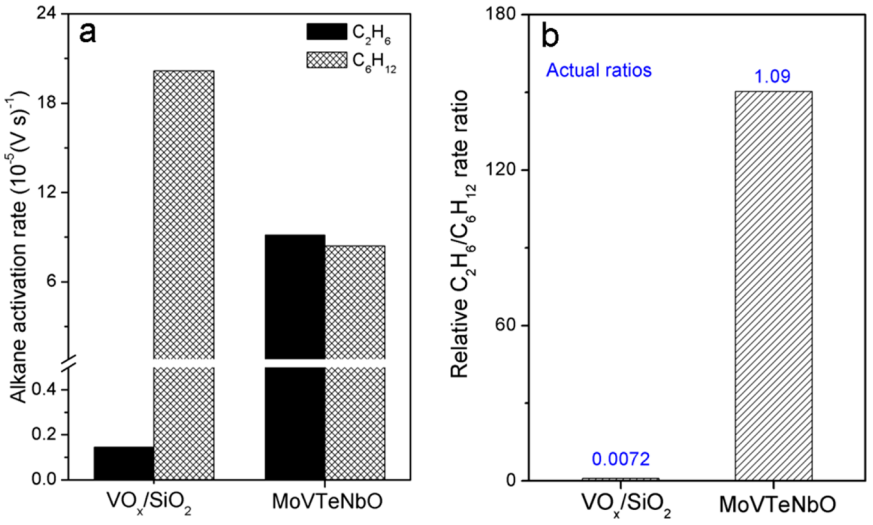

Figure 3. Measured (a) C_2H_6 and C_6H_{12} activation rates on VO_x/SiO_2 and MoVTeNbO, and (b) C_2H_6/C_6H_{12} rate ratios on MoVTeNbO relative to the corresponding values on VO_x/SiO_2 (648 K, 3 kPa C_2H_6 or C_6H_{12}, 3 kPa O_2, 30 cm^3 min^{-1}; 0.4% and 1.7% C_2H_6 and 5% and 8% C_6H_{12} conversions on VO_x/SiO_2 and MoVTeNbO, respectively).

C_2H_6. We conclude from these details that the impurity phases only contribute to external oxide surfaces and any contributions of micropores to the reactivity originate solely from the M1 phase. SEM images of MoVTeNbO samples show plate- and rodlike structures typical of these materials[64,65] (Figure 2b). High resolution TEM of crystallites exhibited a 0.4 nm *d*-spacing, as shown in Figure S5, which is consistent with the separation between (001) planes of M1 phase in XRD measurements (22.1° 2θ in Figure 2a). The XRD pattern of VO_x/SiO_2 shown in Figure S14 indicates the presence of V_2O_5 crystals that do not contain micropores.

N_2 physisorption isotherm measured on a MoVTeNbO sample is shown in Figure 2c. The N_2 uptakes increased steeply with pressure at relative pressures (P/P_0) below 10^{-4} and reached a local plateau indicative of complete filling of micropores (inset in Figure 2c).[40] The uptake at a P/P_0 value of 0.002[40] was 0.56 cm^3 g^{-1} (at standard temperature and pressure), which corresponds to a micropore volume of 7.9×10^{-4} cm^3 g^{-1} and to a micropore internal wall area of 7.9 m^2 g^{-1} for uniform cylindrical pores of 0.4 nm diameter. These measured pore volumes are about an order of magnitude smaller than the theoretical values estimated from all heptagonal pores in the M1 phase,[40] suggesting that the possible blocking of heptagonal pores by metal cations and the presence of impurity phases decrease the fraction of heptagonal pores accessible to reactants but do not completely eliminate it. The uptakes between P/P_0 values 0.05 and 0.35 lead to an external BET surface area of 4.2 m^2 g^{-1} (details in Section S8). Thus, the magnitudes of external surface areas of MoVTeNbO samples are similar to the micropore wall areas and each may contribute to the reactivity of these samples.

Next, we estimate the contributions of the reactive sites in these internal and exposed surfaces to the C_2H_6 activation rates using C_2H_6/C_6H_{12} rate ratios on microporous MoVTeNbO and nonmicroporous VO_x/SiO_2.

3.2. C_2H_6/C_6H_{12} Rate Ratios on VO_x/SiO_2 and MoVTeNbO. *3.2.1. Measured Rate Ratios.* The rates of C_2H_6 and C_6H_{12} reactions are limited by the activation of C−H bonds in intact molecules at O-atoms of oxides.[66] The accessibility of O-atoms at external surfaces and inside heptagonal pores of these molecules on VO_x/SiO_2 and MoVTeNbO are shown in Scheme 2. The VO_x/SiO_2 samples do not impose size restrictions on reactants; therefore, all catalytic O-atoms are considered as external sites equally accessible to C_2H_6 and C_6H_{12}, and the ratio of their activation rates ($r_{C_2H_6}/r_{C_6H_{12}}$) represents merely the ratio of these rates at external sites ($r_{C_2H_6}^{ext}/r_{C_6H_{12}}^{ext}$):

$$\left(\frac{r_{C_2H_6}}{r_{C_6H_{12}}}\right)_{VO_x/SiO_2} = \frac{r_{C_2H_6}^{ext}}{r_{C_6H_{12}}^{ext}} \quad (1)$$

The $r_{C_2H_6}/r_{C_6H_{12}}$ values on VO_x/SiO_2 eliminate the uncertainties inherent to the identification and quantification of active sites on oxides and the effects changes in structure and domain sizes of VO_x[67,68] by providing the same sites for C−H activation steps that limit rates of each reactant. These factors can influence rates of each reaction, but their effects nearly cancel in the ratio. Thus, these values represent the differences between Gibbs free energies of C−H activation at identical surface O-atoms, which depend on the strength and the number of weakest C−H bonds in each molecule.[66,69] In

DOI: 10.1021/acscatal.8b01586
ACS Catal. 2018, 8, 7051−7067

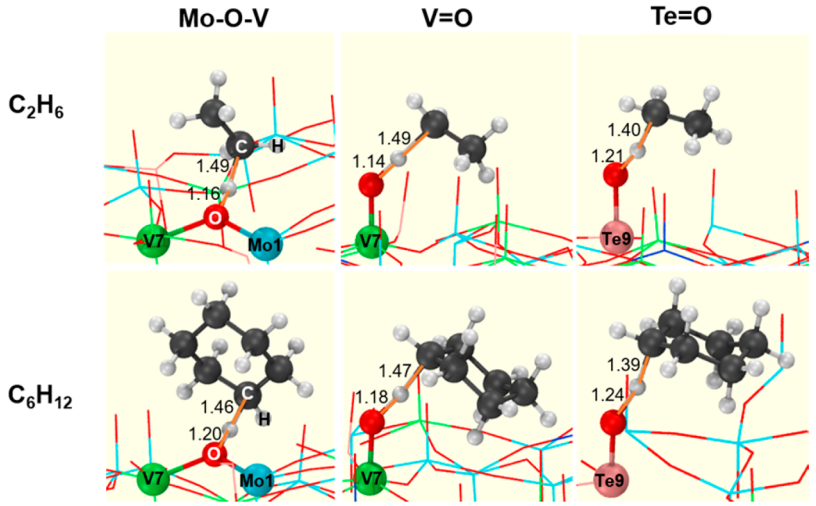

Figure 4. vdW-DF2 derived structures of transition states for C−H activation in C_2H_6 and C_6H_{12} at O-atoms exposed in (001) planes in single-layer MoVTeNbO. The labels on metal centers reflect atom positions shown in Figure 1.

contrast, on MoVTeNbO, C_2H_6 molecules of similar kinetic diameters as the heptagonal pore sizes (0.4 nm)[38] may enter the pores, while C_6H_{12} molecules with much larger kinetic diameters (0.6 nm)[70] are restricted to external surfaces. Thus, the numerator of rate ratios on this catalyst includes additional contribution from sites within the pores ($r_{C_2H_6}^{pore}$):

$$\left(\frac{r_{C_2H_6}}{r_{C_6H_{12}}}\right)_{MoVTeNbO} = \frac{r_{C_2H_6}^{pore} + r_{C_2H_6}^{ext}}{r_{C_6H_{12}}^{ext}} \quad (2)$$

Figure 3a shows C_2H_6 and C_6H_{12} activation rates on VO_x/SiO_2 and MoVTeNbO at a condition that gave <8% hydrocarbon conversions (30 cm^3 min^{-1}, 3 kPa C_2H_6 or C_6H_{12}, 3 kPa O_2, 648 K). These rates lead to rate ratios that are much smaller on VO_x/SiO_2 than on MoVTeNbO (Figure 3b). The absolute value of $r_{C_2H_6}/r_{C_6H_{12}}$ on VO_x/SiO_2 is much lower than unity (0.0072; Figure 3b) because C_2H_6 contains much stronger C−H bonds than C_6H_{12}, which activate at a much lower rate (DFT-derived bond dissociation enthalpy, BDE, 422 and 408 kJ mol^{-1} respectively; Table S6). The $r_{C_2H_6}/r_{C_6H_{12}}$ value on MoVTeNbO is near unity despite this significant bond-strength difference (1.09; Figure 3b). This ratio is 150 times larger than in VO_x/SiO_2 (Figure 3b), which suggests that the $r_{C_2H_6}^{pore}$ term in eq 2 has 2 orders of magnitude larger contribution to the ratios than the values resulting from bond strength differences at identical external sites; therefore, most of the C_2H_6 activations in MoVTeNbO occur within the heptagonal pores.

A different VO_x/SiO_2 sample with much lower weight loading, which results in higher vanadium dispersion, also leads to $r_{C_2H_6}/r_{C_6H_{12}}$ ratios much smaller than unity (0.0055 for 6.5% wt. V_2O_5 on SiO_2; Table S7). Increased dispersion typically leads to decreased V_2O_5 concentrations and increased abundance of oligomeric and monomeric VO_x domains, as determined from Raman spectra.[67,68] Therefore, these data suggest that rate ratios on oxides without micropores are nearly independent of dispersion and of concomitant changes in structure of VO_x domains.

Alternative synthesis procedures described in the Supporting Information yield MoVTeNbO crystals with much higher Te content than the samples described here ($Mo_1V_{0.28}Te_{0.18}Nb_{0.25}$ and $Mo_1V_{0.27}Te_{0.02}Nb_{0.09}$, respectively; Section S2). Yet, both samples lead to high C_2H_6/C_6H_{12} rate ratios, suggesting that Te atoms, which tend to occupy hexagonal pores instead of the heptagonal pores and are partially expelled from crystals during reaction,[15] do not significantly alter the role of heptagonal pores in C_2H_6 turnovers. These results are consistent with only a minor role of Te, as indicated by <13% reported rate enhancements after long times on stream recently attributed to Te removal observed in electron microscopy.[15]

3.2.2. DFT-Derived Rate Constant Ratios on External O-Atoms of MoVTeNbO. The conclusion that C_2H_6/C_6H_{12} rate ratios are near unity because C_2H_6 reactions occur inside heptagonal pores is assessed next using DFT-derived rate ratios on external surfaces of MoVTeNbO simulated by the single layer model shown in Figure 1. The rate-limiting C−H bond activation energies in alkanes, and consequently the alkane activation rates, depend on C−H BDE and the H-atom addition energies (HAE) at O-atoms in oxide catalysts.[69,71,72] Activation energies are typically lower at O-atoms with more negative HAE values, but these values may also be affected by steric hindrance to accessibility of specific O-atoms to large molecules. Therefore, HAE values were calculated for distinct types of O-atoms connected to metal atoms labeled in Figure 1 to identify most reactive sites of each type (HAE values in Table S2). Among metal atoms at the seven-membered rings that form the heptagonal pores, the HAE value was most negative at M1−O−V7 for bridging O-atoms (−269 kJ mol^{-1}) and at V7 = O for terminal O-atoms (−254 kJ mol^{-1}). Away from the heptagonal pores, the HAE values were most negative at Te9 = O (−312 kJ mol^{-1}). The high reactivity of Te = O may reflect artifacts of the single layer model that eliminates more stable Te−O−Te−O chains found in bulk MoVTeNbO.[73] The Te9 = O sites were virtually absent in MoVTeNbO samples ($Mo_1V_{0.27}Te_{0.02}Nb_{0.09}$) and are known to decrease during reactions[15] but are included here to estimate their possible contributions to rate ratios when they are present. The structures of C_2H_6 and C_6H_{12} activation transition states at these three O-atoms (M1−O−V7, V7 = O, and Te9 = O) derived from vdW-DF2 method are shown in Figure 4, and the corresponding activation energies referenced to gas-phase reactants and bare surfaces are shown in Table 1. The

DOI: 10.1021/acscatal.8b01586
ACS Catal. 2018, 8, 7051−7067

Table 1. vdW-DF2 Derived Electronic Energies (ΔE_{TS}), Enthalpy (ΔH_{TS}), and Entropy (ΔS_{TS}) Values (648 K, 1 atm), and Rate Constant Ratios for C_2H_6 and C_6H_{12} Activations (eq 3, 648 K) at O-Atoms Exposed in (001) Planes in Single-Layer MoVTeNbO[a]

O-atom location	reactant	ΔE_{TS} (kJ mol^{-1})	ΔH_{TS} (kJ mol^{-1})	ΔS_{TS} (J mol^{-1}K^{-1})	$k^{ext}_{C_2H_6}/k^{ext}_{C6H_{12}}$
V_7−O−Mo_1	C_2H_6	136	120	−124	8.00×10^{-4}
	C_6H_{12}	110	89	−119	
V_7═O	C_2H_6	139	118	−110	2.11×10^{-4}
	C_6H_{12}	105	79	−106	
Te═O	C_2H_6	109	90	−114	2.05×10^{-3}
	C_6H_{12}	90	64	−108	

[a]ΔH_{TS} and ΔS_{TS} were derived by eqs S22−S32 at 648 K.

electronic energies of activation (ΔE_{TS}) at all three surface O-atoms are larger for C_2H_6 than C_6H_{12} by 19−34 kJ mol^{-1}, consistent with the weaker C−H bonds in the latter molecule. These energies, together with enthalpy (ΔH_{TS}) and entropy (ΔS_{TS}) calculations (Table 1; details in Supporting Information) can be used to estimate ratios of rate constants at external sites:[66,69]

$$\frac{k^{ext}_{C_2H_6}}{k^{ext}_{C_6H_{12}}} = \frac{(n^{C-H} e^{\Delta S_{TS}/R} e^{-\Delta H_{TS}/RT})_{C_2H_6}}{(n^{C-H} e^{\Delta S_{TS}/R} e^{-\Delta H_{TS}/RT})_{C_6H_{12}}} \quad (3)$$

where k^{ext} values represent C−H activation rate constants at an external O-atom in MoVTeNbO, n^{C-H} is the number of C−H bonds in a given molecule (6 for C_2H_6, 12 for C_6H_{12}), R is the universal gas constant, and the subscripts are used to represent reactant molecules. These DFT-derived ratios are much smaller than unity at all three reactive O-atoms on external surfaces at temperatures of experimental rate ratio measurements (<0.002, T = 648 K; Table 1), suggesting that the measured values are near unity (1.09, Figure 3b) on MoVTeNbO samples because C_2H_6 activation occurs predominantly in heptagonal pores which are inaccessible to C_6H_{12}.

Thus, experimental evidence based on rate ratio comparisons with VO_x/SiO_2 as well as computational estimates of rate constant ratios for unconfined molecules at external sites confirm that C_2H_6 activation occurs inside the heptagonal pores of MoVTeNbO. Such confirmations are consistent with rate measurements in analogous MoV oxides of different crystallite sizes that led to ODH rates proportional to micropore volume and independent of external surface area.[39] Next, we examine the elementary steps for ODH and thermodynamic properties of C−H activation steps occurring at external surfaces and pores of VO_x/SiO_2 and MoVTeNbO, respectively, for C_2H_6 and at external surfaces of both oxides for C_6H_{12}.

3.3. Elementary Steps in Oxidative Conversion of C_2H_6 and C_6H_{12}.

The primary and secondary products formed in the oxidative conversion of alkanes and cycloalkanes (C_2H_6 and C_6H_{12}) on metal oxides are shown in Scheme 3. A C−H activation in these molecules leads to alkyl radicals that undergo a second C−H activation to form alkenes as the desired oxidative dehydrogenation (ODH) products. Parallel and sequential O-insertions in alkyl radicals and alkenes, respectively, form oxygenates that ultimately oxidize to CO or CO_2.[61,74]

A sequence of elementary steps consistent with Mars van Krevelen redox cycles for the C_2H_6 ODH on oxides is shown in Scheme 4.[75−78] C_2H_6 in the reactor feed or H_2O formed with increasing conversion along the reactor bed adsorb at lattice O-atoms (MO*) in quasi-equilibrated steps (steps 1 and 1′; Scheme 4). Adsorbed C_2H_6 undergoes an irreversible C−H activation at an O-atom to form a $\bullet C_2H_5$ radical and a surface OH species; a second C−H activation in $\bullet C_2H_5$ forms C_2H_4 and surface OH pairs (OH/MOH*-C_2H_4, step 2). Only the first of these two C−H activations is typically kinetically relevant.[79] The desorption of C_2H_4 and H_2O (Steps 3 and 4; Scheme 4), and sequential irreversible reactions of O-atoms from an O_2 molecule with O-vacancies (M*; steps 5 and 6; Scheme 4) complete the catalytic turnover. These steps and the equilibrium and irreversibility assumptions shown in Scheme 4 lead to an equation that describes the C_2H_6 ODH turnover rate per reactive metal center (M) in the oxide as a function of C_2H_6, O_2, and H_2O pressures (derivations in the Supporting Information):

$$\frac{r_{ODH}}{[M]} = \frac{k_{ODH} K_{ads} P_{C_2H_6}}{1 + K_{ads} P_{C_2H_6} + K'_{ads} P_{H_2O} + \frac{k_{ODH} K_{ads} P_{C_2H_6}}{2k_{ox} P_{O_2}} (1 + K_w P_{H_2O})} \quad (4)$$

where the denominator terms represent ratios of concentrations of MO*, MO*-C_2H_6, MO*-H_2O, M* and OH/MOH* surface species to the MO* concentration, in the

Scheme 3. Primary and Secondary Products Formed in Oxidative Conversion of (a) C_2H_6 and (b) C_6H_{12}

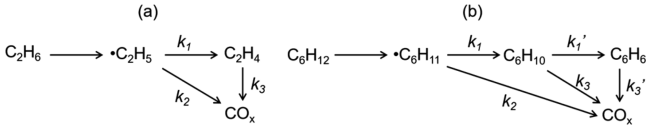

Scheme 4. Proposed Elementary Steps for C_2H_6 ODH at Redox Sites on MoVTeNbO and VO_x/SiO_2[a]

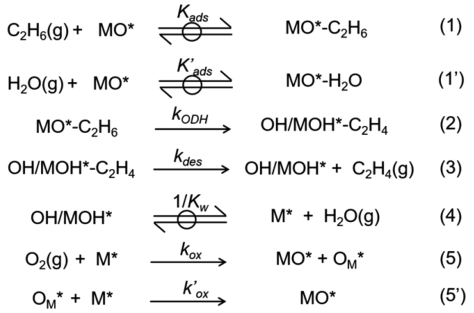

[a]M represents a metal center, which is interpreted as a V-atom in both catalysts.

DOI: 10.1021/acscatal.8b01586
ACS Catal. 2018, 8, 7051−7067

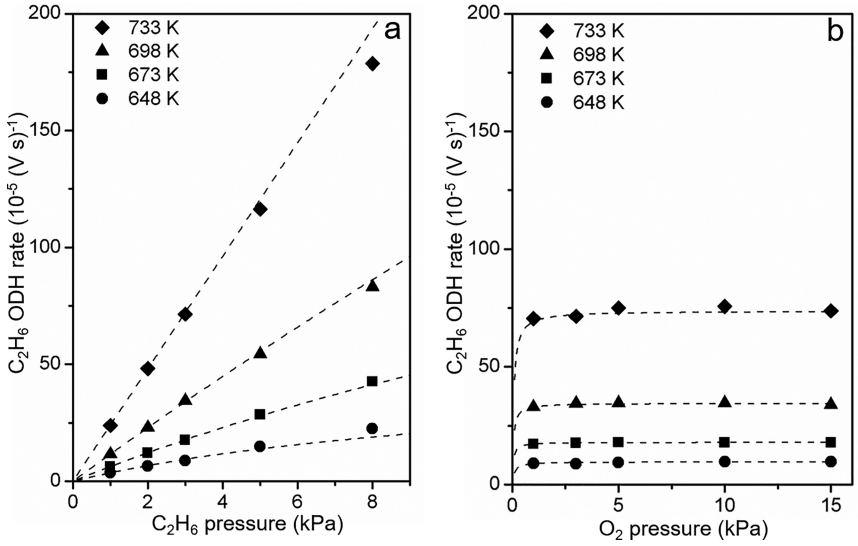

Figure 5. Measured C_2H_6 ODH rates on MoVTeNbO as a function of (a) C_2H_6 pressure at 3 kPa O_2 and (b) O_2 pressure at 3 kPa C_2H_6. Rates were extrapolated to zero conversion using linear fits to the effect of conversion on rates. Dashed curves represent best regression fits to the form eq 5 after replacement of $P_{C_2H_6}$ with $P_{C_6H_{12}}$.

Table 2. Rate and Equilibrium Constants for C_2H_6 and C_6H_{12} ODH Obtained by Regression of Measured Rates to the Form of eq 5 on VO_x/SiO_2 and MoVTeNbO[a]

oxide	temperature (K)	$k_{ODH}K_{ads}$ (10^{-5} V^{-1} kPa^{-1} s^{-1})	K_{ads} (10^{-2} kPa^{-1})	k_{ox} (10^{-5} V^{-1} kPa^{-1} s^{-1})
C_2H_6 ODH				
VO_x/SiO_2	648	0.062 (±0.003)	1.53 (±2.35)	0.21 (±0.06)
	673	0.098 (±0.005)	−2.16 (±2.62)	0.33 (±0.10
	698	0.193 (±0.012)	3.11 (±3.50)	0.57 (±0.20
	733	0.354 (±0.021)	1.33 (±3.27)	1.31 (±0.54
MoVTeNbO	648	3.87 (±0.27)	6.73 (±3.76)	52 (±90)
	673	6.46 (±0.06)	2.60 (±0.52)	208 (±119)
	698	11.7 (±0.2)	0.50 (±0.68)	353 (±249)
	733	24.0 (±0.6)	−0.83 (±1.23)	565 (±562)
C_6H_{12} ODH				
VO_x/SiO_2	588	5.95 (±0.67)	14.4 (±6.4)	4.58 (±0.73)
	603	8.02 (±0.92)	23.1 (±7.0)	7.91 (±1.70)
	623	8.57 (±1.69)	11.2 (±10.7)	11.3 (±5.3)
	648	15.0 (±0.9)	10.9 (±4.7)	16.7 (±5.7)
MoVTeNbO	603	2.07 (±0.34)	11.1 (±9.2)	2.72 (±1.10)
	623	3.62 (±0.40)	9.04 (±6.13)	4.68 (±1.25)
	648	5.88 (±0.83)	5.79 (±7.75)	7.62 (±2.60)
	673	11.6 (±0.6)	3.94 (±2.76)	14.9 (±1.8)

[a]Uncertainties represent two times the standard deviations.

respective order in which they appear in the equation. The k and K values represent rate and equilibrium constants, respectively, for steps shown in Scheme 4.

Analogous elementary steps for C_6H_{12} ODH are shown in Scheme S1, which lead to a rate equation obtained by replacing $P_{C_2H_6}$ in eq 4 with $P_{C_6H_{12}}$, and including additional denominator terms accounting for possible adsorption of C_6H_{12} derived oxygenates at MO* (represented as $K''_{ads}P_{C_6H_xO_y}$; Equation S21).

The radicals formed in step 2 of Scheme 4 (and analogous step in Scheme S1) can alternatively react with surface MOH* or MO* species leading to parallel O-insertion steps that limit selectivity to the alkene products (Scheme 3).[74] The alkenes also undergo O-insertion at surface O-atoms leading to epoxide or aldehyde products. These parallel and sequential products, however, form only after the kinetically relevant first C−H activation required to form the ODH product;[74] therefore, their contributions were included in measured rates to accurately account for primary C−H activation rates.

C_2H_6 and C_6H_{12} ODH rates on undiluted VO_x/SiO_2 and MoVTeNbO samples and on these samples after intrapellet dilution with SiO_2 (1:2 catalyst:diluent weights) are shown in Figure S1. The rates were independent of dilution beyond the batch variations (<20%) in MoVTeNbO grinding and pressing procedures caused potentially by unsystematic changes to crystallite sizes and pore blocking. The electronic energies of intermediate structures for the translation for C_2H_6 molecules in heptagonal pores are also shown in Figure S6. The barriers for such translations are much smaller (<10 kJ mol^{-1}) than C−H activation barriers referenced to the same adsorbed intermediate (172 kJ mol^{-1}). These results and the reported independence of C_2H_6 rates to crystallite sizes in MoV oxides[17]

DOI: 10.1021/acscatal.8b01586
ACS Catal. 2018, 8, 7051−7067

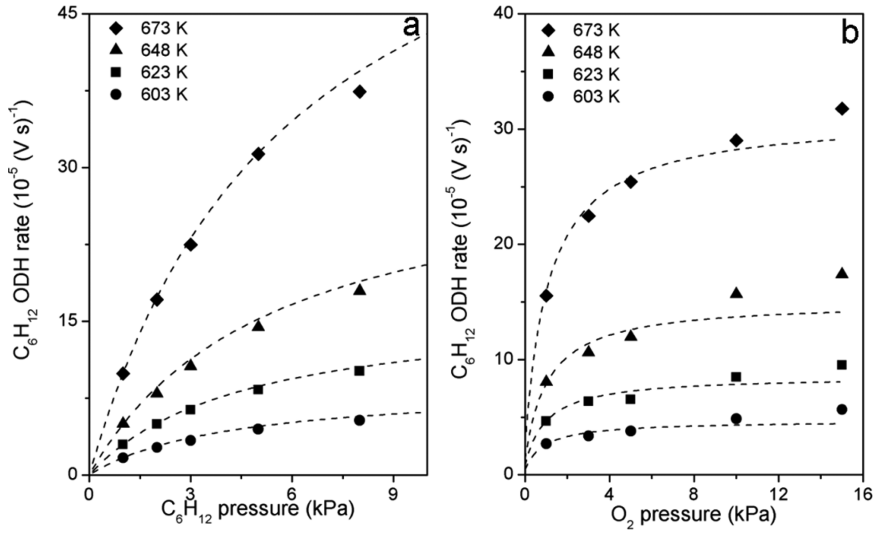

Figure 6. Measured C_6H_{12} ODH rates on MoVTeNbO as a function of (a) C_6H_{12} pressure at 3 kPa O_2 and (b) O_2 pressure at 3 kPa C_6H_{12}. Rates were extrapolated to zero conversion using linear fits to the effect of conversion on rates. Dashed curves represent best regression fits to the form eq 5.

suggest that the measured rates are free of transport artifacts and represent true kinetic limitations on activation of reactants.

The inhibition of reactions by products of oxidative conversion was probed by measuring ODH rates as a function of conversion of reactant hydrocarbons varied by changing residence times, as shown in Figures S7 and S8. Plausible products inhibiting the reactions by blocking reactive sites may include H_2O and C6 oxygenates (shown by denominator terms in eq S21). The decrease in C_2H_6 ODH rates with conversion (Figure S7) was much weaker than the corresponding decrease in C_6H_{12} ODH rates (Figure S8). Such differences in product inhibition may occur because the H_2O molecules formed in both reactions bind weakly to MO* sites at these temperatures,[79] but oxygenates formed in C_6H_{12} oxidations bind more strongly.[80] For both reactions, any effects of product inhibition were removed by extrapolating all rates measured at <15% conversions to zero conversion (Figures S7 and S8). Therefore, all rates reported henceforth reflect ODH rates at the conditions of the reactor inlet free from all products, which simplifies eq 4 to the following form for C_2H_6 ODH rates:

$$\frac{r_{ODH}}{[M]} = \frac{k_{ODH}K_{ads}P_{C_2H_6}}{1 + K_{ads}P_{C_2H_6} + \frac{k_{ODH}K_{ads}P_{C_2H_6}}{2k_{ox}P_{O_2}}} \quad (5)$$

The C_6H_{12} ODH rates can be described by replacing $P_{C_2H_6}$ with $P_{C_6H_{12}}$ in eq 5.

C_2H_6 ODH rates at zero conversions as a function of C_2H_6 and O_2 pressures on MoVTeNbO at 648, 673, 698, and 733 K are shown in Figure 5; analogous effects on VO_x/SiO_2 are shown in Figure S9. These rates increase linearly with C_2H_6 pressure and are independent in O_2 pressure, which suggests that surface coverage of species represented by denominator terms in eq 5 are much smaller than unity at relevant conditions due to weak alkane binding ($K_{ads} \ll 1$ kPa^{-1}) and rapid nature or reoxidation steps ($k_{ox} \gg k_{ODH}K_{ads}$). Regression of these rate data to the functional form of eq 5 gives rate constants ($k_{ODH}K_{ads}$; Table 2) that represent the Gibbs free energy of the C−H activation transition state (G_{TS}) relative to those of uncovered oxide surfaces (G_{MO*}) and gaseous C_2H_6 molecules ($G_{C_2H_{6(g)}}$):

$$k_{ODH}K_{ads} \sim e^{-\Delta G_{TS}/RT} = e^{-(G_{TS}-G_{MO*}-G_{C_2H_6(g)})/RT} \quad (6)$$

C_6H_{12} ODH rates at zero conversions as a function of C_6H_{12} and O_2 pressures on MoVTeNbO at 603, 623, 648, and 673 K are shown in Figure 6; analogous effects on VO_x/SiO_2 are shown in Figure S10. The C_6H_{12} ODH rates increased linearly with C_6H_{12} pressures at low pressures but exhibited sublinearity at high C_6H_{12} pressures. These nonlinear effects suggest that adsorbed C_6H_{12} derived species or reduced centers occupy significant fractions of surface sites at high C_6H_{12} pressure (eq 5 analog for C_6H_{12}). The $k_{ODH}K_{ads}$ values obtained by regression of the rate data to the form of eq 5 represent the Gibbs free energies of the C−H activation transition states with respect to uncovered oxide surfaces and gaseous C_6H_{12} molecules. The values of rate and equilibrium constants on VO_x/SiO_2 and MoVTeNbO are shown in Table 2. Next, we examine the differences in C−H activation enthalpies and entropies between C_2H_6 and C_6H_{12} on both oxides to assess the role of micropores in stabilizing transition states for C_2H_6 activation.

3.4. Influence of Pore Environment on C−H Activation Energy. *3.4.1. Measured Activation Enthalpies and Entropies.* The Gibbs free energy change in eq 6 reflects contributions from activation enthalpy and entropy ($\Delta G_{TS} = \Delta H_{TS} - T\Delta S_{TS}$), which can be expressed in the form of the Eyring-Polanyi equation:[81,82]

$$\ln\left(\frac{k_{ODH}K_{ads}h}{k_BT}\right) = \frac{\Delta S_{TS}}{R} - \frac{\Delta H_{TS}}{RT} \quad (7)$$

where h and k_B represent the Planck and Boltzmann constants, respectively. The $\ln(k_{ODH}K_{ads}h/k_BT)$ values derived from measured rate constants for C_2H_6 and C_6H_{12} on VO_x/SiO_2 and MoVTeNbO (Table 2) are shown as a function of reciprocal temperatures in Figure 7. The regression of these data to the form of eq 7 leads to enthalpies and entropies for C−H activation transition states relative to gaseous reactants, which are shown in Table 3.

DOI: 10.1021/acscatal.8b01586
ACS Catal. 2018, 8, 7051−7067

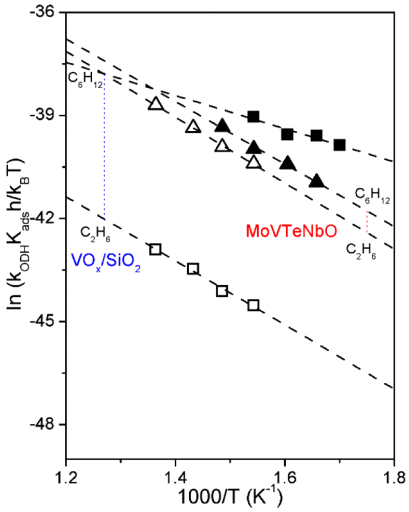

Figure 7. Measured ODH rate constants for activation of the C_2H_6 (open symbols) and C_6H_{12} (closed symbols) as a function of reciprocal temperature on VO_x/SiO_2 (squares) and MoVTeNbO (triangles). Dashed lines represent best regression fits to the form of eq 7.

Table 3. Measured Activation Enthalpy (ΔH) and Entropy (ΔS) for Alkane ODH Reactions on MoVTeNbO and VO_x/SiO_2[a]

oxide	reactant	ΔH (kJ mol^{-1})	ΔS (J^{-1} mol^{-1} K^{-1})
VO_x/SiO_2	C_2H_6	78 (±10)	−251 (±15)
	C_6H_{12}	40 (±17)	−263 (±28)
MoVTeNbO	C_2H_6	79 (±5)	−213 (±7)
	C_6H_{12}	76 (±9)	−215 (±14)

[a]Uncertainties represent two times the standard deviations.

On VO_x/SiO_2 catalysts, activation enthalpy is significantly larger for C_2H_6 (78 ± 10 kJ mol^{-1}) than for C_6H_{12} (40 ± 17 kJ mol^{-1}), consistent with the weaker C−H bonds in the C_6H_{12} (C−H BDE 422 and 408 kJ mol^{-1}; Table S6). The C_6H_{12} activation enthalpy is higher on MoVTeNbO than VO_x/SiO_2, suggesting that O-atoms of MoVTeNbO are less reactive due to weaker H-abstraction ability of its O-atoms. In contrast to VO_x/SiO_2, however, C_2H_6 activation enthalpy (79 ± 5 kJ mol^{-1}) on MoVTeNbO more closely resembles the C_6H_{12} activation enthalpy (76 ± 9 kJ mol^{-1}), despite weaker C−H bonds in the latter molecule. The rate ratios examined above confirmed that most of the C_2H_6 reactions occur within the micropores (Figure 3b); thus, the lower activation enthalpy difference between C_2H_6 and C_6H_{12} on MoVTeNbO is consistent with the stabilization of C_2H_6 molecules by van der Waals (vdW) interactions with surfaces confining the molecules within these micropores, as often observed in zeotype materials.[83] The concentrations of active sites within micropores and the external surfaces on MoVTeNbO are not identical, which may slightly influence entropy differences between C_2H_6 and C_6H_{12} activations derived from Figure 7. Without accounting for these effects, however, the entropy losses are larger for C_2H_6 (relative to C_6H_{12}) in MoVTeNbO than VO_x/SiO_2, which is consistent with fewer degrees of freedom for C_2H_6 transition states confined in pores. The effects of confinement are probed next using DFT calculations for C_2H_6 activation within MoVTeNbO pores.

3.4.2. DFT Estimates for vdW Stabilization of C_2H_6 ODH in Pores. The energies of intermediates and transition states for C−H activation in C_2H_6 inside a heptagonal pore of bulk MoVTeNbO (Figure 1, double-layer model) as a function of reaction coordinate are shown in Figure 8. C−H activations here transfer H-atoms to the Mo1−O−V7 bridging O-atoms (Figure 1), which is the most reactive O-atom accessible inside the pore (HAE = −269 kJ mol^{-1}; Table S2). The energies were derived using PBE functionals that do not account for vdW interactions and the vdW-DF2 functionals that incorporate rigorous empirical vdW corrections. Comparisons of these methods reveal contributions from vdW stabilization as well as steric repulsion to tightly confined molecules in heptagonal pores.

In the initial stable adsorption position inside the heptagonal pore, the C_2H_6 molecule is aligned with the plane of an oxide layer (C_2H_6 translation calculations in Figure S6). The PBE-derived adsorption for this structure is slightly endothermic (ΔE_{ads}^{PBE} = +16 kJ mol^{-1}), suggesting that the heptagonal pore imposes slight steric repulsion between electron densities in C_2H_6 and intrapore surfaces. These repulsions are offset by stabilizing vdW forces, leading to vdW-DF2 adsorption energy that is exothermic and more negative than PBE by 76 kJ mol^{-1} ($\Delta E_{ads}^{vdW-DF2}$ = −60 kJ mol^{-1}). The effects of vdW stabilization are preserved to a large extent in the C_2H_6 C−H activation transition states, which are more stable with vdW-DF2 than PBE by 55 kJ mol^{-1} (ΔE_{TS}^{PBE} = +167 kJ mol^{-1}; $\Delta E_{TS}^{vdW-DF2}$ = +112 kJ mol^{-1}; Figure 8). After C−H activation, the •C_2H_5 translates within the pore to a position between two oxide

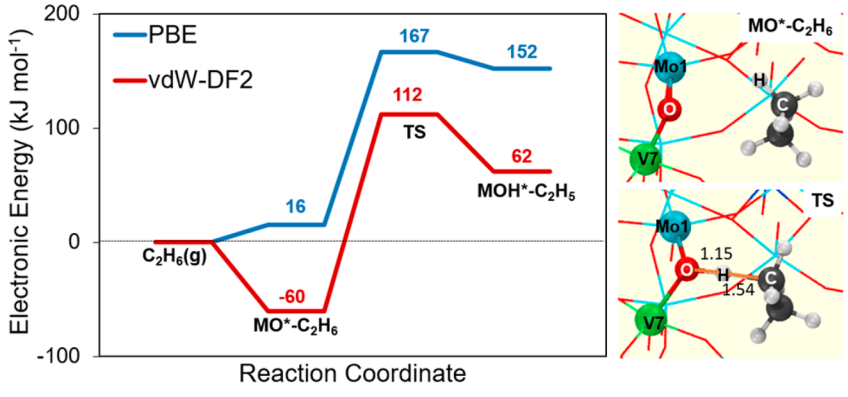

Figure 8. PBE and vdW-DF2 derived energies and vdW-DF2 derived structures for adsorbed C_2H_6 and C−H activation transition state at Mo1−O−V7 location in heptagonal pores of double-layer MoVTeNbO shown in Figure 1.

DOI: 10.1021/acscatal.8b01586
ACS Catal. 2018, 8, 7051−7067

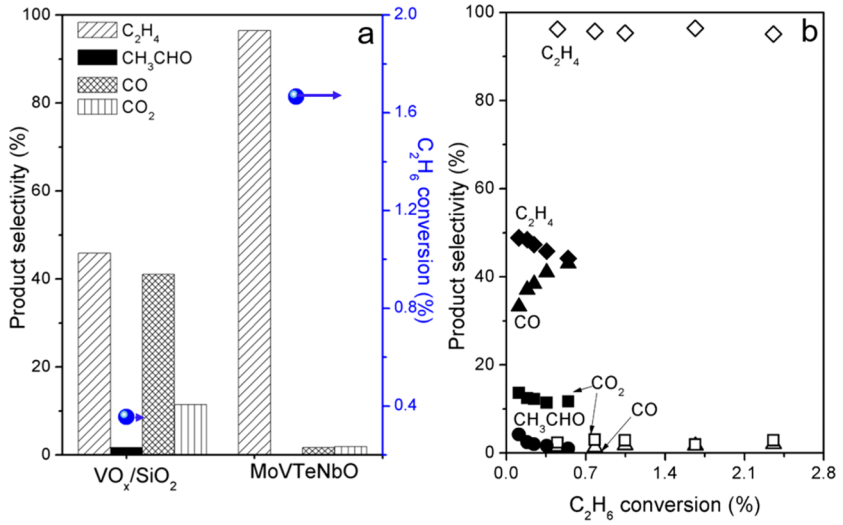

Figure 9. (a) C_2H_6 conversion and product selectivity at 30 cm^3 min^{-1} flow rate and (b) product selectivity as a function of C_2H_6 conversion on VO_x/SiO_2 (closed symbols in b) and MoVTeNbO (open symbols in b), at 648 K, 3 kPa C_2H_6, 3 kPa O_2.

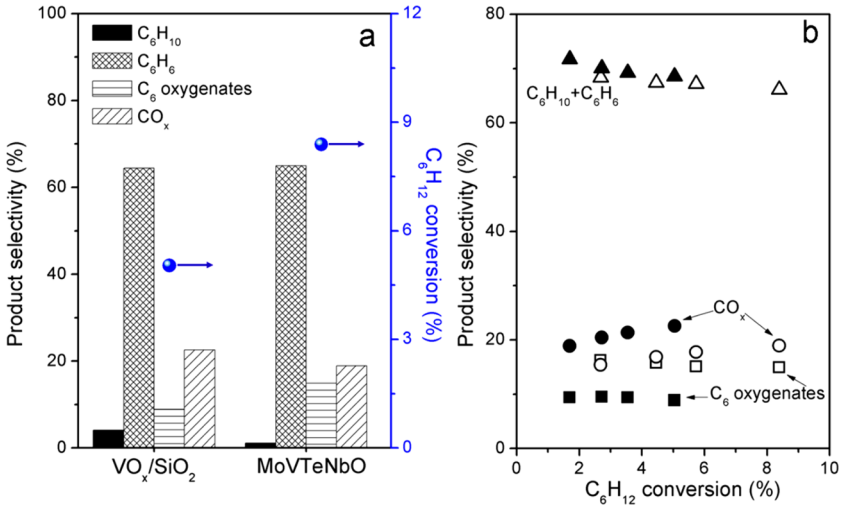

Figure 10. (a) C_6H_{12} conversion and product selectivity at 30 cm^3 min^{-1} flow rate and (b) product selectivity as a function of C_6H_{12} conversion on VO_x/SiO_2 (closed symbols in b) and MoVTeNbO (open symbols in b), at 648 K, 3 kPa C_6H_{12}, 3 kPa O_2.

layers, which leads to a further increased stability difference between the two methods ($\Delta E^{PBE}_{\bullet C_2H_5}$ = +152 kJ mol^{-1}; $\Delta E^{vdW-DF2}_{\bullet C_2H_5}$ = +62 kJ mol^{-1}; Figure 8). The significant vdW stabilization at the C−H activation transition state drives most C_2H_6 activations to occur within the heptagonal pore, in spite of abundant external O-atoms in MoVTeNb oxides, as demonstrated by measured rate ratios and vdW-DF2 derived activation energies at Mo1−O−V7 that are lower inside the pores than at external sites on the single-layer external surface model (112 kJ mol^{-1}, Figure 8; 136 kJ mol^{-1}, Table 1). Such stabilizations in pores are also consistent with a lower measured activation enthalpy difference between C_2H_6 and C_6H_{12} on MoVTeNbO than on VO_x/SiO_2 (Table 3; Figure 7) because C_2H_6 activation occurs inside the pores of MoVTeNbO.

3.5. Influence of the Pore Environment on the Selectivity to ODH Products. *3.5.1. Selectivity at External Surfaces and Micropores for VO_x/SiO_2 and MoVTeNbO.* The selectivity to C_2H_4 ($S_{C_2H_4}$) and other products in C_2H_6 oxidative conversion at a standard condition (30 cm^3 min^{-1}) and as a function of C_2H_6 conversion ($X_{C_2H_6}$) for different C_2H_6 residence times is shown in Figure 9 (3 kPa C_2H_6 and O_2, 648 K). The MoVTeNbO samples exhibited much higher selectivity to C_2H_4 (96% $S_{C_2H_4}$ at 1.8% $X_{C_2H_6}$; Figure 9a) than VO_x/SiO_2 (45% $S_{C_2H_4}$ at 0.3% $X_{C_2H_6}$; Figure 9a). Furthermore, the $S_{C_2H_4}$ value in MoVTeNbO decreased much less sensitively with increasing conversion than in VO_x/SiO_2 (Figure 9b), consistent with the well-known selective nature of these bulk mixed oxides and moderately selective nature[84] of VO_x/SiO_2.

In contrast to C_2H_6 product selectivity trends, the selectivity to dehydrogenation products of C_6H_{12} (C_6H_{10} and C_6H_6) are similar on MoVTeNbO and VO_x/SiO_2 at standard conditions (30 cm^3 min^{-1}, 3 kPa C_6H_{12} and O_2, 648 K; Figure 10a) and change similarly with conversion (Figure 10b). These trends suggest that the external surfaces of both catalysts are similarly selective to ODH products (C_6H_{10} and C_6H_6), and the high selectivity for C_2H_6 ODH on MoVTeNbO is conferred specifically by some property of the heptagonal pores. The similar selectivity values at external surfaces may reflect that V_2O_5 domains in high loading 41% wt. VO_x/SiO_2 and

DOI: 10.1021/acscatal.8b01586
ACS Catal. 2018, 8, 7051−7067

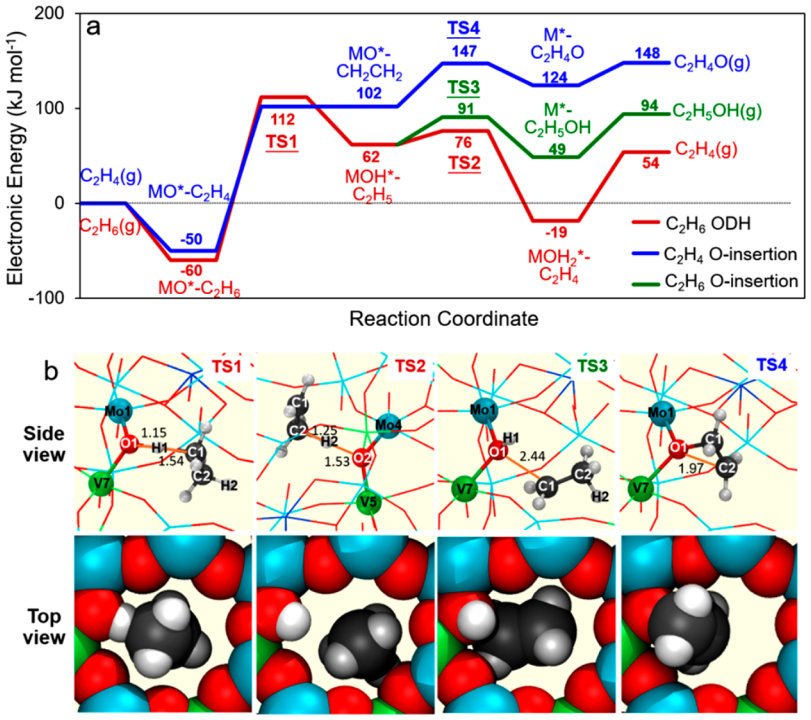

Figure 11. (a) vdW-DF2 derived electronic energies and (b) structures of intermediates and transition states for C_2H_6 ODH, parallel O-insertion in $\bullet C_2H_5$ and sequential O-insertion in C_2H_4 at O-atoms exposed in heptagonal pores of double layer MoVTeNbO. The labels on metal centers reflect atom positions shown in Figure 1. Relevant bond distances are listed in Tables S3 and S4.

Table 4. vdW-DF2 Derived Electronic Energies (ΔE), Enthalpies (ΔH), Entropies (ΔS) of Intermediates and Transition States for C_2H_6 ODH, Parallel O-Insertion, and Sequential C_2H_4 O-Insertion at O-Atoms Exposed in Heptagonal Pores of Double Layer MoVTeNbO[a]

intermediates or transition states	ΔE (kJ mol $^{-1}$)	ΔH (kJ mol $^{-1}$)	ΔS (J mol $^{-1}$ K^{-1})
C_2H_6 ODH and parallel O-insertion			
MO*-C_2H_6	−60	−55	−117
TS1	112	99	−139
MOH*-C_2H_5	62	63	−98
TS2	76	64	−130
OH/MOH*-C_2H_4	−18	−13	−106
C_2H_4 (g)	54	55	18
TS3	91	91	−142
MC_2H_5OH*	49	62	−149
C_2H_5OH (g)	94	98	30
sequential C_2H_4 O-insertion			
MO*-C_2H_4	−50	−43	−124
MOCH_2CH_2*	102	109	−145
TS4	147	151	−169
MC_2H_4O*	124	136	−167
C_2H_4O (g)	148	150	12

[a] ΔH and ΔS were derived by eqs S22−S32 at 648 K.

MoVTeNb oxides contain similar V oxo distorted octahedra as the most reactive sites for C_6H_{12}, but pores impart separate unique factors to enhance C_2H_4 selectivity for C_2H_6 ODH.

Mole balance on products formed in reactions in Scheme 3 suggests that the value of $S_{C_2H_4}$ extrapolated to zero conversion from measured selectivity trends represents the fraction of primary C−H activations that branch toward C_2H_4 formation instead of O-insertion to $\bullet C_2H_5$ radicals (near 100% $S_{C_2H_4}$ at zero $X_{C_2H_6}$ implies $k_2/k_1 \ll 1$ in Scheme 3). Similarly, the slope of selectivity versus conversion plots represents rates of secondary reactions relative to C_2H_4 formation (small $-dS_{C_2H_4}/dX_{C_2H_6}$ implies small k_3/k_1 in Scheme 3). The smaller rates of parallel and sequential O-insertion steps (k_2 and k_3 in Scheme 3) relative to the desired dehydrogenation steps (k_1), suggest that pore environments hinder O-insertions. These possibilities are examined next using DFT calculations.

3.5.2. C−H Activation and O-Insertion Pathways in Micropores. The vdW-DF2 derived electronic energies and structures of intermediates and transition states for C−H activation and O-insertion in C_2H_6 and C_2H_4 inside the heptagonal pores of MoVTeNbO are shown in Figure 11.

DOI: 10.1021/acscatal.8b01586
ACS Catal. 2018, 8, 7051−7067

Enthalpy and entropy estimates for these species are shown in Table 4. The $\bullet C_2H_5$ radical species formed from C_2H_6 via C−H activation at Mo1−O−V7 O-atom (ΔE_{TS1} = 112 kJ mol^{-1}; Figures 8, 11) undergo a second C−H activation at Mo4−O−V5 O-atom in another layer of the bulk oxide to form C_2H_4; the second transition state energy is much lower (ΔE_{TS2} = 76 kJ mol^{-1}; Figure 11), which is consistent with the assumption that the first C−H activation is the rate-limiting step in ODH (section 3.3). The $\bullet C_2H_5$ radical can alternatively rebound to a surface MOH* species to form adsorbed C_2H_5OH via a transition state that has a higher energy than the C_2H_4 formation transition state (ΔE_{TS3} = 91 kJ mol^{-1}; Figure 11). The external surfaces of oxides tend to exhibit lower electronic energy barriers for C_2H_5OH formation than C_2H_4,[85] yet ethanol formation rates at typical reaction conditions are lower than alkene formation due to rapid O_2 activation steps that leave low MOH* concentrations for radical rebound.[85] Here, based on higher electronic energies, C_2H_5OH formation rates will be even lower inside the pores, which is consistent with low k_2/k_1 values (Scheme 3) suggested by the high measured selectivity at zero conversion (Figure 9b).

The ODH product C_2H_4 contains much stronger C−H bonds than C_2H_6, which limits its secondary reactions via C−H activation. The C_2H_4 molecules can instead undergo rapid sequential reactions to form either ethylene epoxide or acetaldehyde.[86−88] Each of these two possible sequential paths requires an initial C_2H_4 adsorption via C−O bond formation.[86−88] The adsorption energies and the barriers for subsequent formation of O-inserted products are much lower than primary C−H activation on oxide catalysts,[86−88] which makes these sequential reactions the most significant limitation on attaining high selectivity to C_2H_4.[79] In contrast to conventional oxides, the electronic energies for C_2H_4 adsorption inside the heptagonal pores are nearly as high as the C−H activation barriers ($\Delta E_{MOCH_2CH_{2^*}}$ = 102 kJ mol^{-1} ∼ ΔE_{TS1} = 112 kJ mol^{-1}; Figure 11), which together with increased zero-point vibrational energy due to the additional C−O bond formation make the adsorbed C_2H_4 intermediate less stable than the C−H activation transition state ($\Delta H_{MOCH_2CH_{2^*}}$ = 109 kJ mol^{-1} ∼ ΔH_{TS1} = 99 kJ mol^{-1}; Figure 11; Table 4). This inhibits the undesired O-insertion steps, leading to high selectivity in MoVTeNbO heptagonal pores ($k_3/k_1 \ll 1$ apparent from slopes in C_2H_4 selectivity trends; Figure 9b). The transition states for epoxide and acetaldehyde formation present higher barriers than the C_2H_4 adsorption energy (ΔE_{TS4} = 145 kJ mol^{-1}; Figure 11; ΔE_{TS6} = 108 kJ mol^{-1}, Figure S11), which confirms that these steps are favored less than C−H activation steps in heptagonal pores.

The hindrance to O-insertion inside heptagonal pores appears to originate from tight confinement of C_2H_6 and C_2H_4 inside these pores. C−H bond activation requires the transfer of a small H-atom to the O-atoms within the heptagonal pores, and therefore, the steric hindrances are weaker than the benefits of vdW stabilization, as indicated by lower activation energy at Mo1−O−V7 in the bulk model than the single-layer external surface model (ΔE^{pore}_{TS1} = 112 kJ mol^{-1}, Table 4; ΔE^{ext}_{TS1} = 136 kJ mol^{-1}, Table 1). In contrast, the C−O bond formation in O-insertion steps requires much bulkier CH_2 groups to attain closer contact with concave pore walls than the reactant molecules, as shown by the top views of transition states in Figure 11, which significantly enhance steric hindrances. Indeed, C_2H_4 molecules adsorb by forming C−O bonds at the same O-atom sites on external surfaces of MoVTeNbO with much lower adsorption energy than the heptagonal pores via configurations that are inaccessible inside the pores, as shown in the Supporting Information ($\Delta E^{pore}_{MOCH_2CH_{2^*}}$ = 102 kJ mol^{-1}, Table 4; $\Delta E^{ext}_{MOCH_2CH_{2^*}}$ = 14 kJ mol^{-1}, Figure S12). Thus, the heptagonal pores enhance selectivity to alkenes by enhancing C−H activation rates and suppressing O-insertions via a combination of vdW and steric effects, as summarized in Scheme 5.

Scheme 5. Influence of Confinement in Heptagonal Pores on C−H Activation and O-Insertion Steps

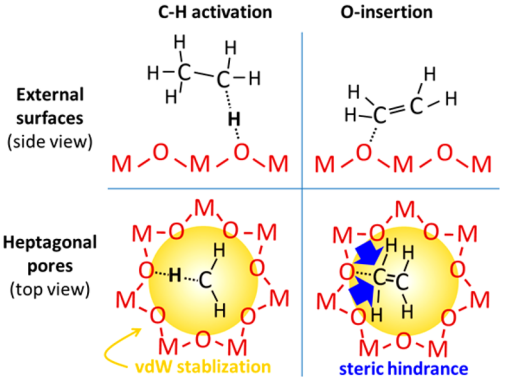

The selectivity enhancements imparted by greater enthalpic stabilization of C−H activation steps in heptagonal pores are in part offset by fewer degrees of freedom in molecules inside the pores than outside and lead to greater entropy loss. The contribution of entropy to Gibbs free energy is greater at higher temperatures, which favors reactions on external surfaces. Such effects are evident in the measured MoVTeNbO to VO_x/SiO_2 ratios for the C_2H_6/C_6H_{12} activation rate constant ratios as a function of temperature shown in Figure S13. Thus, the selectivity enhancements imparted by pore environments are more effective at lower temperature, which is consistent with the high C_2H_4 yields attained in these materials at much lower temperatures (∼653 K) than other selective C_2H_6 ODH processes (>900 K) and betrays the uniqueness of the functioning of these materials.[1]

The insights from experiment and theory capture the essential role of the structural features of complex MoVTeNb oxides in selective C_2H_6 ODH and demonstrate how pore environments can steer catalytic transformations to enhance selectivity even beyond those achieved by selecting the best elemental compositions of metal oxides. The effects of confinement are well-known in zeotype materials; their important roles in such mixed oxides were, however, not fully identified. The current findings strengthen and advance the previous heuristic concepts of site isolation in mixed oxides that guided the initial discovery and improvement of mixed oxides,[89] by providing more rigorous molecular connection of localization and isolation of molecules in pores to the selectivity enhancement. Such insights may provide important guidance to the development of improved selective oxidation catalysts by using dispersion and steric forces as some of the design parameters.

MoVTeNbO materials have also been studied extensively for selective oxidation and ammoxidation of C_3H_8 to oxygenates and nitriles, respectively.[13,32] The C_3H_8 molecules have slightly larger kinetic diameters than C_2H_6,[90] suggesting a tighter

DOI: 10.1021/acscatal.8b01586
ACS Catal. 2018, 8, 7051−7067

guest−host fit with possible diffusion limitation and restriction of C−H activation to O-atoms near pore mouths. The product C_3H_6 molecules contain weak allylic C−H bonds that readily undergo C−H activation and subsequent allylic O-insertions, which may exhibit different site requirements than C_2H_6 dehydrogenation or O-insertion at the C=C bond in C_2H_4. The roles of external surfaces and mixed phases of oxides have been extensively reported for such reactions.[89] Even in this case, the preference for C−H activation in alkanes near pores or pore-mouths may play a significant role in reactivity and selectivity because catalysts containing M1 phase oxides can perform these steps more selectively than other oxides using the C_3H_8 feed instead of C_3H_6. More detailed investigations of these plausible roles of pores in such selective oxidations in M1 phase containing catalysts will be performed in the future.

4. CONCLUSIONS

The ratio of C_2H_6 to C_6H_{12} activation rates in oxidative conversion on microporous MoVTeNbO and nonmicroporous VO_x/SiO_2 oxides is used to examine the role of micropores in ODH catalysis. The rate ratio on VO_x/SiO_2 is much smaller than unity, which is consistent with the stronger C−H bond in C_2H_6. The rate ratio is significantly higher on MoVTeNbO than VO_x/SiO_2, which indicates high C_2H_6 turnover rates occur within the pores relative to external surfaces. DFT-derived rate constant ratios on external surfaces of MoVTeNbO are also much smaller than unity, which confirms that external surfaces are not responsible for the experimentally observed high rate ratio on MoVTeNbO. Kinetic data are consistent with elementary steps based on Mars-van Krevelen redox cycles with kinetically relevant C−H activation steps. The measured activation enthalpy difference between C_2H_6 and C_6H_{12} is much lower on MoVTeNbO than VO_x/SiO_2, which is consistent with DFT-derived activation enthalpies accounting for van der Waals interactions. This difference suggests that C_2H_6 is stabilized by van der Waals interactions within the pores.

VO_x/SiO_2 and MoVTeNbO exhibit similar C_6H_{12} oxidation product selectivities under the same conditions and C_6H_{12} conversion, while for C_2H_6 oxidation, the selectivity to C_2H_4 was much higher on the latter oxide. These trends suggest that external surfaces of both oxides are similarly selective to C−H activation and O-insertion products, but micropores in MoVTeNb are more selective to C−H activation products. The electronic energies for the C_2H_6 oxidation reaction pathways confirm that the rate-limiting C−H activation transition states are stabilized in the micropores, while the intermediates and transition states involved in O-insertion reactions are destabilized by steric hindrance caused by concave curvature inside the tightly confining pores.

■ ASSOCIATED CONTENT

Supporting Information

The Supporting Information is available free of charge on the ACS Publications website at DOI: 10.1021/acscatal.8b01586.

Definitions of ODH rate and selectivity; alternate synthesis procedure for MoVTeNbO; influence of catalyst dilution and time on stream and reactant conversion on ODH rates; density of states in MoVTeNbO; atomic arrangements in M1, M2, and Mo_5O_{14} phases; TEM images of MoVTeNbO; micropore area and BET area estimations from N_2 adsorption isotherms; barriers for translation of C_2H_6 in heptagonal pores; elementary steps and derivations for ODH rate equations; effect of C_2H_6, C_6H_{12}, and O_2 pressure on ODH rates on VO_x/SiO_2; statistical mechanics treatments for enthalpy and entropy calculations; C−H BDE and HAE values at O-atoms of MoVTeNbO; energies, structures, and bond distances for intermediates and transition states; effect of temperature on size selectivity of MoVTeNbO; effect of VO_x loading percentage on C_2H_6 to C_6H_{12} rate ratios; and XRD pattern of 41% wt. VO_x/SiO_2 (PDF)

■ AUTHOR INFORMATION

Corresponding Author

*E-mail: prashant.deshlahra@tufts.edu. Tel: +1-617-627-7972. Fax: +1-617-627-3991.

ORCID

Leelavathi Annamalai: 0000-0001-8207-1424

Steven L Suib: 0000-0003-3073-311X

Prashant Deshlahra: 0000-0002-1063-4379

Author Contributions

‖L.A. and Y.L. contributed equally.

Notes

The authors declare no competing financial interest.

■ ACKNOWLEDGMENTS

Financial support from Tufts Collaborates grant and Tufts Faculty Research Fund is gratefully acknowledged. Computational resources were provided by the Extreme Science and Engineering Discovery Environment[91] (proposals CTS150005 and CHE140066), which is supported by the National Science Foundation Grant ACI-1548562 and the Tufts High Performance Cluster. We are grateful to Prof. Maria Flytzani-Stephanopoulos, Prof. E. Charles H. Sykes, and Dr. James Vlahakis for helpful discussions. S.L.S. acknowledges support of the US Department of Energy, Office of Basic Energy Sciences, Division of Chemical, Biological and Geological Sciences under Grant DE-FG02-86ER13622.A000 for support of this research.

■ REFERENCES

(1) *The Changing Landscape of Hydrocarbon Feedstocks for Chemical Production*; Alper, J., Ed.; National Academies Press: Washington, DC, 2016.

(2) Cavani, F.; Ballarini, N.; Cericola, A. Oxidative Dehydrogenation of Ethane and Propane: How Far from Commercial Implementation? *Catal. Today* **2007**, *127*, 113−131.

(3) Cavalcanti, F. A. P.; Han, S.; Klugherz, P. D.; Lemonds, A. M.; Martenak, D. J.; Vickery, E. M.; Zolotorofe, D. L. Regeneration of Mixed Metal Oxide Catalysts. U.S. Patent 7,538,059, May 26, 2009.

(4) Arnold, S. C.; Gaffney, A. M.; Song, R.; Yeh, C. Y. Process for Producing Ethylene via Oxidative Dehydrogenation (ODH) of Ethane. U.S. Patent 8,519,210, August 27, 2013.

(5) Nieto, J. L.; Botella, P.; Vázquez, M.; Dejoz, A. The Selective Oxidative Dehydrogenation of Ethane over Hydrothermally Synthesised MoVTeNb Catalysts. *Chem. Commun.* **2002**, 1906−1907.

(6) Botella, P.; García-González, E.; Dejoz, A.; López Nieto, J. M.; Vázquez, M. I.; González-Calbet, J. Selective Oxidative Dehydrogenation of Ethane on MoVTeNbO Mixed Metal Oxide Catalysts. *J. Catal.* **2004**, *225*, 428−438.

(7) Thorsteinson, E.; Wilson, T.; Young, F.; Kasai, P. The Oxidative Dehydrogenation of Ethane over Catalysts Containing Mixed Oxides of Molybdenum and Vanadium. *J. Catal.* **1978**, *52*, 116−132.

DOI: 10.1021/acscatal.8b01586
ACS Catal. 2018, 8, 7051−7067

(8) Burch, R.; Swarnakar, R. Oxidative Dehydrogenation of Ethane on Vanadium-Molybdenum Oxide and Vanadium-Niobium-Molybdenum Oxide Catalysts. *Appl. Catal.* **1991**, *70*, 129−148.
(9) Ruth, K.; Burch, R.; Kieffer, R. Mo−V−Nb Oxide Catalysts for the Partial Oxidation of Ethane: II. Chemical and Catalytic Properties and Structure Function Relationships. *J. Catal.* **1998**, *175*, 27−39.
(10) Grasselli, R. K.; Buttrey, D. J.; DeSanto, P.; Burrington, J. D.; Lugmair, C. G.; Volpe, A. F.; Weingand, T. Active Centers in Mo-V-Te-Nb-O_x (amm) Oxidation Catalysts. *Catal. Today* **2004**, *91−92*, 251−258.
(11) Chiu, C.-c.; Vogt, T.; Zhao, L.; Genest, A.; Rösch, N. Structure and Electronic Properties of MoVO Type Mixed-Metal Oxides−A Combined View by Experiment and Theory. *Dalton Trans.* **2015**, *44*, 13778−13795.
(12) Ushikubo, T.; Oshima, K.; Kayou, A.; Vaarkamp, M.; Hatano, M. Ammoxidation of Propane over Catalysts Comprising Mixed Oxides of Mo and V. *J. Catal.* **1997**, *169*, 394−396.
(13) Ushikubo, T.; Oshima, K.; Kayo, A.; Umezawa, T.; Kiyono, K.-i.; Sawaki, I. Process for Producing Nitriles. U.S. Patent 5,281,745, Jan 1994.
(14) Bettahar, M.; Costentin, G.; Savary, L.; Lavalley, J. On the Partial Oxidation of Propane and Propylene on Mixed Metal Oxide Catalysts. *Appl. Catal., A* **1996**, *145*, 1−48.
(15) Zhu, Y.; Sushko, P. V.; Melzer, D.; Jensen, E.; Kovarik, L.; Ophus, C.; Sanchez-Sanchez, M.; Lercher, J. A.; Browning, N. D. Formation of Oxygen Radical Sites on $MoVNbTeO_x$ by Cooperative Electron Redistribution. *J. Am. Chem. Soc.* **2017**, *139*, 12342−12345.
(16) Trunschke, A.; Noack, J.; Trojanov, S.; Girgsdies, F.; Lunkenbein, T.; Pfeifer, V.; Hävecker, M.; Kube, P.; Sprung, C.; Rosowski, F.; Schlögl, R. The Impact of the Bulk Structure on Surface Dynamics of Complex Mo-V-based Oxide Catalysts. *ACS Catal.* **2017**, *7*, 3061−3071.
(17) Ishikawa, S.; Ueda, W. Microporous Crystalline Mo-V Mixed Oxides for Selective Oxidations. *Catal. Sci. Technol.* **2016**, *6*, 617−629.
(18) Fu, G.; Xu, X.; Sautet, P. Vanadium Distribution in Four-Component Mo-V-Te-Nb Mixed-Oxide Catalysts from First Principles: How to Explore the Numerous Configurations? *Angew. Chem.* **2012**, *124*, 13026−13030.
(19) Vogt, T.; Blom, D.; Jones, L.; Buttrey, D. ADF-STEM Imaging of Nascent Phases and Extended Disorder within the Mo-V-Nb-Te-O Catalyst System. *Top. Catal.* **2016**, *59*, 1489−1495.
(20) Melzer, D.; Xu, P.; Hartmann, D.; Zhu, Y.; Browning, N. D.; Sanchez-Sanchez, M.; Lercher, J. A. Atomic-Scale Determination of Active Facets on the MoVTeNb Oxide M1 Phase and Their Intrinsic Catalytic Activity for Ethane Oxidative Dehydrogenation. *Angew. Chem., Int. Ed.* **2016**, *55*, 8873−8877.
(21) Cheng, M.-J.; Goddard, W. A. The Mechanism of Alkane Selective Oxidation by the M1 phase of Mo-V-Nb-Te Mixed Metal Oxides: Suggestions for Improved Catalysts. *Top. Catal.* **2016**, *59*, 1506−1517.
(22) Lwin, S.; Diao, W.; Baroi, C.; Gaffney, A. M.; Fushimi, R. R. Characterization of $MoVTeNbO_x$ Catalysts during Oxidation Reactions using In Situ/Operando Techniques: A Review. *Catalysts* **2017**, *7*, 109.
(23) Védrine, J. C. Heterogeneous Partial (amm) Oxidation and Oxidative Dehydrogenation Catalysis on Mixed Metal Oxides. *Catalysts* **2016**, *6*, 22−48.
(24) Albonetti, S.; Cavani, F.; Trifiro, F. Key Aspects of Catalyst Design for the Selective Oxidation of Paraffins. *Catal. Rev.: Sci. Eng.* **1996**, *38*, 413−438.
(25) Muthukumar, K.; Yu, J.; Xu, Y.; Guliants, V. V. Propane Ammoxidation Over the Mo-V-Te-Nb-O M1 Phase: Reactivity of Surface Cations in Hydrogen Abstraction Steps. *Top. Catal.* **2011**, *54*, 605−613.
(26) Murayama, H.; Vitry, D.; Ueda, W.; Fuchs, G.; Anne, M.; Dubois, J. L. Structure Characterization of Orthorhombic Phase in MoVTeNbO Catalyst by Powder X-ray diffraction and XANES. *Appl. Catal., A* **2007**, *318*, 137−142.
(27) DeSanto, P., Jr.; Buttrey, D. J.; Grasselli, R. K.; Lugmair, C. G.; Volpe, A. F.; Toby, B. H.; Vogt, T. Structural Characterization of the Orthorhombic Phase M1 in MoVNbTeO Propane Ammoxidation Catalyst. *Top. Catal.* **2003**, *23*, 23−38.
(28) Shiju, N. R.; Liang, X.; Weimer, A. W.; Liang, C.; Dai, S.; Guliants, V. V. The Role of Surface Basal Planes of Layered Mixed Metal Oxides on Selective Transformation of Lower Alkanes: Propane Ammoxidation over Surface ab Planes of Mo-V-Te-Nb-O M1 Phase. *J. Am. Chem. Soc.* **2008**, *130*, 5850−5851.
(29) Ueda, W.; Vitry, D.; Katou, T. Crystalline MoVO Based Complex Oxides as Selective Oxidation Catalysts of Propane. *Catal. Today* **2005**, *99*, 43−49.
(30) Korovchenko, P.; Shiju, N. R.; Dozier, A. K.; Graham, U. M.; Guerrero-Pérez, M. O.; Guliants, V. V. M1 to M2 Phase Transformation and Phase Cooperation in Bulk Mixed Metal Mo-V-M-O (M = Te, Nb) Catalysts for Selective Ammoxidation of Propane. *Top. Catal.* **2008**, *50*, 43−51.
(31) Li, X.; Buttrey, D. J.; Blom, D. A.; Vogt, T. Improvement of the Structural Model for the M1 Phase Mo-V-Te-Nb-O Propane (amm) Oxidation Catalyst. *Top. Catal.* **2011**, *54*, 614−626.
(32) Hävecker, M.; Wrabetz, S.; Kröhnert, J.; Csepei, L.-I.; d'Alnoncourt, R. N.; Kolen'ko, Y. V.; Girgsdies, F.; Schlögl, R.; Trunschke, A. Surface Chemistry of Phase-Pure M1MoVTeNb Oxide During Operation in Selective Oxidation of Propane to Acrylic Acid. *J. Catal.* **2012**, *285*, 48−60.
(33) Chen, X.; Yang, Q.; Chu, B.; An, H.; Cheng, Y. Valence Variation of Phase-pure M1MoVNbTe Oxide by Plasma Treatment for Improved Catalytic Performance in Oxidative Dehydrogenation of Ethane. *RSC Adv.* **2015**, *5*, 91295−91301.
(34) Guliants, V. V.; Bhandari, R.; Swaminathan, B.; Vasudevan, V. K.; Brongersma, H. H.; Knoester, A.; Gaffney, A. M.; Han, S. Roles of Surface Te, Nb, and Sb Oxides in Propane Oxidation to Acrylic Acid over Bulk Orthorhombic Mo− V− O Phase. *J. Phys. Chem. B* **2005**, *109*, 24046−24055.
(35) Guliants, V. V.; Bhandari, R.; Brongersma, H. H.; Knoester, A.; Gaffney, A. M.; Han, S. A Study of the Surface Region of the Mo−V− Te− O Catalysts for Propane Oxidation to Acrylic Acid. *J. Phys. Chem. B* **2005**, *109*, 10234−10242.
(36) Guliants, V. V.; Brongersma, H. H.; Knoester, A.; Gaffney, A. M.; Han, S. Surface Active Sites Present in the Orthorhombic M1 Phases: Low Energy Ion Scattering Study of Methanol and Allyl Alcohol Chemisorption over Mo−V−Te−Nb−O and Mo−V−O Catalysts. *Top. Catal.* **2006**, *38*, 41−50.
(37) Callahan, J.; Grasselli, R. A Selectivity Factor in Vapor-Phase Hydrocarbon Oxidation Catalysis. *AIChE J.* **1963**, *9*, 755−760.
(38) Ishikawa, S.; Yi, X.; Murayama, T.; Ueda, W. Heptagonal Channel Micropore of Orthorhombic Mo_3VO_x as Catalysis Field for the Selective Oxidation of Ethane. *Appl. Catal., A* **2014**, *474*, 10−17.
(39) Ishikawa, S.; Yi, X.; Murayama, T.; Ueda, W. Catalysis Field in Orthorhombic Mo_3VO_x Oxide Catalyst for the Selective Oxidation of Ethane, Propane and Acrolein. *Catal. Today* **2014**, *238*, 35−40.
(40) Sadakane, M.; Kodato, K.; Kuranishi, T.; Nodasaka, Y.; Sugawara, K.; Sakaguchi, N.; Nagai, T.; Matsui, Y.; Ueda, W. Molybdenum-Vanadium-Based Molecular Sieves with Microchannels of Seven-Membered Rings of Corner-Sharing Metal Oxide Octahedra. *Angew. Chem., Int. Ed.* **2008**, *47*, 2493−2496.
(41) Sadakane, M.; Ohmura, S.; Kodato, K.; Fujisawa, T.; Kato, K.; Shimidzu, K.-i.; Murayama, T.; Ueda, W. Redox Tunable Reversible Molecular Sieves: Orthorhombic Molybdenum Vanadium Oxide. *Chem. Commun.* **2011**, *47*, 10812−10814.
(42) Tatsumi, T.; Nakamura, M.; Negishi, S.; Tominaga, H.-o. Shape-Selective Oxidation of Alkanes with H_2O_2 Catalysed by Titanosilicate. *J. Chem. Soc., Chem. Commun.* **1990**, 476−477.
(43) Yokoyama, H.; Kobayashi, H.; Hasegawa, J.-y.; Fukuoka, A. Selective Dehydration of Mannitol to Isomannide over Hβ Zeolite. *ACS Catal.* **2017**, *7*, 4828−4834.
(44) Canlas, C. P.; Lu, J.; Ray, N. A.; Grosso-Giordano, N. A.; Lee, S.; Elam, J. W.; Winans, R. E.; Van Duyne, R. P.; Stair, P. C.;

DOI: 10.1021/acscatal.8b01586
ACS Catal. 2018, 8, 7051−7067

Notestein, J. M. Shape-Selective Sieving Layers on an Oxide Catalyst Surface. *Nat. Chem.* **2012**, *4*, 1030−1036.
(45) Sanfiz, A. C.; Hansen, T. W.; Girgsdies, F.; Timpe, O.; Rödel, E.; Ressler, T.; Trunschke, A.; Schlögl, R. Preparation of Phase-Pure M1MoVTeNb Oxide Catalysts by Hydrothermal Synthesis-Influence of Reaction Parameters on Structure and Morphology. *Top. Catal.* **2008**, *50*, 19−32.
(46) Valente, J. S.; Armendáriz-Herrera, H. c.; Quintana-Solórzano, R.; del Ángel, P.; Nava, N.; Massó, A.; López Nieto, J. M. Chemical, Structural, and Morphological Changes of a MoVTeNb Catalyst During Oxidative Dehydrogenation of Ethane. *ACS Catal.* **2014**, *4*, 1292−1301.
(47) Kresse, G.; Hafner, J. Ab Initio Molecular Dynamics for Liquid Metals. *Phys. Rev. B: Condens. Matter Mater. Phys.* **1993**, *47*, 558−561.
(48) Kresse, G.; Furthmüller, J. Efficiency of Ab-Initio Total Energy Calculations for Metals and Semiconductors Using a Plane-Wave Basis Set. *Comput. Mater. Sci.* **1996**, *6*, 15−50.
(49) Kresse, G.; Furthmüller, J. Efficient Iterative Schemes for Ab Initio Total-Energy Calculations Using a Plane-Wave Basis Set. *Phys. Rev. B: Condens. Matter Mater. Phys.* **1996**, *54*, 11169−11186.
(50) Lee, K.; Murray, É. D.; Kong, L.; Lundqvist, B. I.; Langreth, D. C. Higher-Accuracy Van der Waals Density Functional. *Phys. Rev. B: Condens. Matter Mater. Phys.* **2010**, *82*, 081101−081104.
(51) Klimeš, J.; Bowler, D. R.; Michaelides, A. Van der Waals Density Functionals Applied to Solids. *Phys. Rev. B: Condens. Matter Mater. Phys.* **2011**, *83*, 195131.
(52) Perdew, J. P.; Burke, K.; Ernzerhof, M. Generalized Gradient Approximation Made Simple. *Phys. Rev. Lett.* **1996**, *77*, 3865−3868.
(53) Kresse, G.; Joubert, D. From Ultrasoft Pseudopotentials to the Projector Augmented-Wave Method. *Phys. Rev. B: Condens. Matter Mater. Phys.* **1999**, *59*, 1758−1775.
(54) Sofo, J.; Mahan, G. Electronic Structure of $CoSb_3$: A Narrow-Band-Gap Semiconductor. *Phys. Rev. B: Condens. Matter Mater. Phys.* **1998**, *58*, 15620−15623.
(55) Monkhorst, H. J.; Pack, J. D. Special Points for Brillouin-Zone Integrations. *Phys. Rev. B: Condens. Matter Mater. Phys.* **1976**, *13*, 5188−5192.
(56) Jónsson, H.; Mills, G.; Jacobsen, K. W. In *Classical and Quantum Dynamics in Condensed Phase Simulations*; Berne, B. J., Ciccotti, G., Coker, D. F., Eds.; World Scientific: Singapore, 1998; pp 385−404.
(57) Henkelman, G.; Jónsson, H. A Dimer Method for Finding Saddle Points on High Dimensional Potential Surfaces Using Only First Derivatives. *J. Chem. Phys.* **1999**, *111*, 7010−7022.
(58) McQuarrie, D. *Statistical Mechanics*; University Science Books: Sausalito, CA, 2000.
(59) Campbell, C. T.; Sellers, J. R. V. Enthalpies and Entropies of Adsorption on Well-Defined Oxide Surfaces: Experimental Measurements. *Chem. Rev.* **2013**, *113*, 4106−4135.
(60) Ivars, F.; Solsona, B.; Hernández, S.; Nieto, J. M. L. Influence of Gel Composition in the Synthesis of MoVTeNb Catalysts Over Their Catalytic Performance in Partial Propane and Propylene Oxidation. *Catal. Today* **2010**, *149*, 260−266.
(61) Argyle, M. D.; Chen, K.; Bell, A. T.; Iglesia, E. Effect of Catalyst Structure on Oxidative Dehydrogenation of Ethane and Propane on Alumina-Supported Vanadia. *J. Catal.* **2002**, *208*, 139−149.
(62) DeSanto, P.; Buttrey, D. J.; Grasselli, R. K.; Lugmair, C. G.; Volpe, A. F.; Toby, B. H.; Vogt, T. Structural Aspects of the M1 and M2 Phases in MoVNbTeO Propane Ammoxidation Catalysts. *Z. Kristallogr. - Cryst. Mater.* **2004**, *219*, 152−165.
(63) Kardash, T. Y.; Plyasova, L. M.; Bondareva, V. M.; Andrushkevich, T. V.; Dovlitova, L. S.; Ischenko, A. I.; Nizovskii, A. I.; Kalinkin, A. V. M_5O_{14}-Like V-Mo-Nb Oxide Catalysts: Structure and Catalytic Performance. *Appl. Catal., A* **2010**, *375*, 26−36.
(64) Grasselli, R.; Lugmair, C.; Volpe, A. Towards an Understanding of the Reaction Pathways in Propane Ammoxidation Based on the Distribution of Elements at the Active Centers of the M1 phase of the MoV (Nb, Ta) TeO System. *Top. Catal.* **2011**, *54*, 595−604.
(65) Oshihara, K.; Hisano, T.; Ueda, W. Catalytic Oxidative Activation of Light Alkanes Over Mo−V-Based Oxides Having Controlled Surface. *Top. Catal.* **2001**, *15*, 153−160.
(66) Zboray, M.; Bell, A. T.; Iglesia, E. Role of C-H Bond Strength in the Rate and Selectivity of Oxidative Dehydrogenation of Alkanes. *J. Phys. Chem. C* **2009**, *113*, 12380−12386.
(67) Carrero, C.; Schlögl, R.; Wachs, I.; Schomaecker, R. Critical Literature Review of the Kinetics for the Oxidative Dehydrogenation of Propane over Well-Defined Supported Vanadium Oxide Catalysts. *ACS Catal.* **2014**, *4*, 3357−3380.
(68) Carrero, C. A.; Keturakis, C. J.; Orrego, A.; Schomäcker, R.; Wachs, I. E. Anomalous Reactivity of Supported V_2O_5 Nanoparticles for Propane Oxidative Dehydrogenation: Influence of the Vanadium Oxide Precursor. *Dalton Trans.* **2013**, *42*, 12644−12653.
(69) Deshlahra, P.; Iglesia, E. Reactivity and Selectivity Descriptors for the Activation of C-H Bonds in Hydrocarbons and Oxygenates on Metal Oxides. *J. Phys. Chem. C* **2016**, *120*, 16741−16760.
(70) Muller, J. A.; Conner, W. C. Cyclohexane in ZSM 5. 1. FTIR and X-ray Studies. *J. Phys. Chem.* **1993**, *97*, 1451−1454.
(71) Deshlahra, P.; Iglesia, E. Toward More Complete Descriptors of Reactivity in Catalysis by Solid Acids. *ACS Catal.* **2016**, *6*, 5386−5392.
(72) Deshlahra, P.; Carr, R. T.; Chai, S.-H.; Iglesia, E. Mechanistic Details and Reactivity Descriptors in Oxidation and Acid Catalysis of Methanol. *ACS Catal.* **2015**, *5*, 666−682.
(73) Ceriotti, M.; Pietrucci, F.; Bernasconi, M. Ab Initio Study of the Vibrational Properties of Crystalline TeO_2: The α, β, and γ Phases. *Phys. Rev. B: Condens. Matter Mater. Phys.* **2006**, *73*, 104304−104317.
(74) Rozanska, X.; Sauer, J. Oxidative Conversion of C1−C3 Alkanes by Vanadium Oxide Catalysts. DFT Results and Their Accuracy. *Int. J. Quantum Chem.* **2008**, *108*, 2223−2229.
(75) Klose, F.; Joshi, M.; Hamel, C.; Seidel-Morgenstern, A. Selective Oxidation of Ethane Over a VO_x/γ-Al_2O_3 Catalyst − Investigation of the Reaction Network. *Appl. Catal., A* **2004**, *260*, 101−110.
(76) Creaser, D.; Andersson, B. Oxidative Dehydrogenation of Propane Over V-Mg-O: Kinetic Investigation by Nonlinear Regression Analysis. *Appl. Catal., A* **1996**, *141*, 131−152.
(77) Mars, P.; van Krevelen, D. W. Oxidations Carried Out by Means of Vanadium Oxide Catalysts. *Chem. Eng. Sci.* **1954**, *3*, 41−59.
(78) Choksi, T.; Greeley, J. Partial Oxidation of Methanol on MoO_3 (010): A DFT and Microkinetic Study. *ACS Catal.* **2016**, *6*, 7260−7277.
(79) Argyle, M. D.; Chen, K.; Bell, A. T.; Iglesia, E. Ethane Oxidative Dehydrogenation Pathways on Vanadium Oxide Catalysts. *J. Phys. Chem. B* **2002**, *106*, 5421−5427.
(80) Birky, T. W.; Kozlowski, J. T.; Davis, R. J. Isotopic Transient Analysis of the Ethanol Coupling Reaction Over Magnesia. *J. Catal.* **2013**, *298*, 130−137.
(81) Eyring, H. The Activated Complex in Chemical Reactions. *J. Chem. Phys.* **1935**, *3*, 107−115.
(82) Evans, M. G.; Polanyi, M. Some Applications of the Transition State Method to the Calculation of Reaction Velocities, Especially in Solution. *Trans. Faraday Soc.* **1935**, *31*, 875−894.
(83) Gounder, R.; Iglesia, E. The Catalytic Diversity of Zeolites: Confinement and Solvation Effects within Voids of Molecular Dimensions. *Chem. Commun.* **2013**, *49*, 3491−3509.
(84) Klisińska, A.; Samson, K.; Gressel, I.; Grzybowska, B. Effect of Additives on Properties of V_2O_5/SiO_2 and V_2O_5/MgO Catalysts: I. Oxidative Dehydrogenation of Propane and Ethane. *Appl. Catal., A* **2006**, *309*, 10−16.
(85) Rozanska, X.; Fortrie, R.; Sauer, J. Oxidative Dehydrogenation of Propane by Monomeric Vanadium Oxide Sites on Silica Support. *J. Phys. Chem. C* **2007**, *111*, 6041−6050.
(86) Dai, G.-L.; Li, Z.-H.; Lu, J.; Wang, W.-N.; Fan, K.-N. Deep Oxidations in the Oxidative Dehydrogenation Reaction of Propane Over V_2O_5 (001): Periodic Density Functional Theory Study. *J. Phys. Chem. C* **2012**, *116*, 807−817.

DOI: 10.1021/acscatal.8b01586
ACS Catal. 2018, 8, 7051−7067

(87) Guoliang, D.; Zhenhua, L.; Wenning, W.; Jing, L.; Kangnian, F. Periodic DFT Study of the Deep Oxidation in the Oxidative Dehydrogenation of Ethane Over V_2O_5 (001). *Chin. J. Catal.* **2013**, *34*, 906−910.
(88) Liu, J.; Mohamed, F.; Sauer, J. Selective Oxidation of Propene by Vanadium Oxide Monomers Supported on Silica. *J. Catal.* **2014**, *317*, 75−82.
(89) Grasselli, R. K. Site Isolation and Phase Cooperation: Two Important Concepts in Selective Oxidation Catalysis: A Retrospective. *Catal. Today* **2014**, *238*, 10−27.
(90) Krokidas, P.; Castier, M.; Moncho, S.; Brothers, E.; Economou, I. G. Molecular Simulation Studies of the Diffusion of Methane, Ethane, Propane, and Propylene in ZIF-8. *J. Phys. Chem. C* **2015**, *119*, 27028−27037.
(91) Towns, J.; Cockerill, T.; Dahan, M.; Foster, I.; Gaither, K.; Grimshaw, A.; Hazlewood, V.; Lathrop, S.; Lifka, D.; Peterson, G. D.; et al. XSEDE: Accelerating Scientific Discovery. *Comput. Sci. Eng.* **2014**, *16*, 62−74.

DOI: 10.1021/acscatal.8b01586
ACS Catal. 2018, 8, 7051−7067